

# Towards a More Renewable Energy Based LFC under Random Packet Transmissions and Delays with Stochastic Generation and Demand

Deepak Kumar Panda, Saptarshi Das, *Member, IEEE*, Stuart Townley

**Abstract**—The load frequency control (LFC) aims to keep the frequency fluctuation of the power grids within certain specified limits, under various load disturbances. However, with the increased usage of renewable energy sources (RES) in smart grids, it is essential to regulate the conventional power plants, based on renewable energy penetration levels. Moreover, with the decentralized nature of the control operation in smart grids, the communication network between the control center and actuator faces the challenge of random communication delays, packet drops in the form of cyber-attacks. In this paper, the conventional thermal power plant operations within an LFC has been modified using energy storage elements with an emphasis on maximizing the RES utilization while tackling the problems associated with cyber-physical systems like packet drops and random time delays. A filtered proportional-integral-derivative (PID) controller is tuned in the LFC using the particle swarm optimization (PSO) algorithm, including random time delays and cyber-attacks modelled as random packet drops. The tuned PID control performance in the LFC scheme is tested with synthetic stochastic as well as real profiles of RES and load demands. The numerical analysis has been conducted on two area LFC model with Monte-Carlo simulations of stochastic demand and generation profiles.

**Note to Practitioners**—We are moving towards more renewable energy-based cyber-physical power grids, and it is becoming increasingly important to understand the limits of the balance between more renewable energy integration vs changing the prime-mover in thermal power generation units to meet uncertain load demands. This paper proposes a new LFC scheme employing a nonlinear dead-zone element between the control signals and the actuators (prime movers) which allows the utilization of the available RES to meet the load and then send a set-point change command in the thermal power generators if the RES does not meet the load. The robustness of the smart grid stability is also verified with the denial of service (DoS) type cyber-attack which is represented in the form of high probability of packet drops and stochastic time delays in the communication channels between the control center and the generation units. It is also essential to understand how different stochastic profiles may affect the stability and performance of the tuned LFC loops, under random time delays and packet dropouts. These are quantified using the uncertainty bounds of grid frequency, its rate of change, control inputs and power exchange between the two areas which are analyzed using Monte Carlo simulations with different types of nonstationary load and RES profiles, and also using real data to

show the effectiveness of the LFC scheme with communication constraints and the resulting imperfections.

**Index Terms**—Load frequency control, optimization, energy storage, renewable energy, nonstationary signals, packet drops

## I. INTRODUCTION

THE utility industries are now facing several operational challenges with the increasing usage of RES. With the focus on reducing the dependence on fossil fuels, several technical and economic feasibility studies have been conducted on 100% renewable usage taking the case of New Zealand [1], Nordic Countries [2], Caribbean island [3], Macedonia [4], Denmark [5], [6], Ireland [7], Japan [8], United States [9] and United Kingdom [10], with the optimal usage of hydro, wind, geothermal and energy storage devices. In [9], analysis is performed concerning the country's economy and global climate cost reduction per person. However, with the increasing integration of RES, it is becoming essential to study the implications on the dynamics of the smart grids which can be studied using various LFC schemes.

### A. Previous Works on LFC with Renewable Energy/Storage

Several standalone hybrid power systems for LFC have been described in [11]–[13],[12], [14], consisting of wind and solar power with various storage devices operating in linear and nonlinear regimes. Electric vehicles (EVs) as storage devices with nonlinear functionality has been used within LFC in [15], [16]. A combination of the traditional multi-area LFC scheme and RES has been investigated by incorporating wind power systems [17], [18] and solar photovoltaic (PV) in [19], [20]. Data driven and forecasting approaches for LFC are adopted in [21]–[23] by making necessary changes in the secondary control loop and facilitating inter-area communication between the operators. Real wind profile data has been used in [22] for stochastic power system LFC models. Changes in the control loop has been facilitated in [24] which decouples the balancing act from the system dynamics. The primary control loop has been used in frequency restoration while secondary control

Manuscript received September 26, 2019; revised October 10, 2020; July 17, 2020; May 17, 2020; accepted December 01, 2020. SD was partially supported by the ESIF ERDF Cornwall New Energy project, project number: 05R16P00282.

The authors are with the Department of Mathematics, College of Engineering, Mathematics and Physical Sciences, University of Exeter, Penryn

Campus, Cornwall TR10 9FE, UK (e-mail: dp457@exeter.ac.uk, saptarshi.das@ieee.org, S.B.Townley@exeter.ac.uk). S. Das is also with the Institute for Data Science and Artificial Intelligence, University of Exeter, Laver Building, North Park Road, Exeter, Devon EX4 4QE, UK. S. Townley is also with the Environment and Sustainability Institute, University of Exeter, Penryn Campus, Cornwall TR10 9FE, UK.

activation is required only in the case of specific local events. The solar and wind power generation along with load demands have been considered as stochastic models in [11], [13], [25] where the stochastic natures of the inputs are described using synthetic profiles as filtered random numbers with drifts and jumps. However, in these cases, the system consists of RES acting as stochastic input variables along with the storage devices as actuators to damp out the grid oscillations. Filtered white noise is used to model the wind velocities in [26] to control the pitch angle of the wind turbine system.

### B. Previous Works on LFC with Time Delays/Packet Dropouts

Open communication channels and the decentralized nature of the controllers in power plants and smart grids can cause communication delays, which are detrimental to the LFC performance. Delay dependent stability of LFC is analyzed using sliding mode control [14], and decentralized fuzzy  $H_\infty$  control [27] for variable time delays and system uncertainties and multi-area power systems with nonlinear constraints [28]. Nonconvex optimization methods are adopted in [29], [30] for designing PID controller in time-delayed LFC systems. The LFC has been modelled as an interval power system in [31] using Kharitonov's theorem where the controller's robustness was tested with governor dead-band, generator rate constraint and communication time delays.

The interrupted packet transmission in industrial automation and process control have been introduced in the form of DoS attack which attempts to reduce the system availability by denying the information exchange between the sensor to controller and controller to actuator respectively. Event-triggered methods are used in [32]–[34] for LFC. According to this scheme, the information is transmitted if the control signals meet a specific criterion. In [32]–[34], the event triggering strategy has been modified for LFC to make the communication system robust to the interrupted data transmission induced by the DoS attacks. Resilient controllers for LFC have been designed using the autoencoder extreme learning machine in [35]. Further methods for mitigating cyberattacks have been described using hierarchical games between the transmitter and the attacker in [36], using a delay estimator and decision-making unit in [37] and zero input actuator policy in [38]. Combinations of time delays and DoS attacks are described in [39] where the latter is modelled via attack duration and frequency, which has uniform upper and lower bounds.

### C. Contributions of this Paper over Existing Literature

This paper combines the whole system complexities posed by the controller communication network like the DoS attacks modelled by random interruption of data packets and random time delays due to its decentralized nature of the operation. So far the existing works have incorporated either DoS cyberattacks or time delays in the control loops except in [39] where analytical stability is obtained for a less complicated LFC scheme. The DoS attacks modelled in the existing works are bounded by duration and frequency. The work done in this paper eliminates the need for a predictor and an estimator for the lost data packets. Moreover, it does not need a change in the existing communication networks to handle these complexities

of random time delays or DoS cyberattacks as dropped out control signal packets. Performance robustness is obtained by tuning the PID controllers in each area using particle swarm optimization (PSO) considering the presence of time delay and cyberattack in the simulation model as an adversarial tuning mechanism for resilient control design. The robustness of the controller in the cyber-physical system is tested using the stochastic profiles including stationary (i.e. Gaussian) and nonstationary inputs, e.g. geometric Brownian motion (gBm) and fractional Brownian motion (fBm), which are simulated by solving stochastic differential equations (SDEs) as discussed in [40]. The results are also validated with the real profiles of solar, wind and load demand. Several energy storage elements are also added in the hybrid power system, as shown in Figure 1, as per the schemes in [41] and [11].

The main contributions of this paper are as follows:

- Tuning the filtered PID controllers for two-area LFC with energy storage devices using PSO on a more realistic and complex smart grid model considering random time delays and DoS cyberattacks in the form of high data packet interruptions from the controllers to the actuators. Also, higher system complexities involve different types of nonlinearities (rate constraints and output saturations) in the storage elements and the control loops. Post-hoc analysis of the control performance of the tuned LFC system and convergence characteristics of the optimization-based controller design is also investigated.
- Comparison of the frequency and rate of change of frequency (ROCOF) fluctuations for varying random packet transmission rate and random time delays. The control performances are also compared with stationary, nonstationary and real input profiles as per the IEEE grid standards [42] recommended for connecting distributed energy resources to the grid.
- Comparison of other important grid operational measures in case of different RES and load profiles, e.g. storage operations and RES penetration level into the smart grid as well as visualizing the uncertainties on these grid performance measures using Monte Carlo simulations.
- Insights into the LFC system operations using bivariate statistical analysis of the smart grid operational variables. Also, carrying out nonparametric hypothesis tests on the signal norms of the grid frequency fluctuations for two areas and tie-line power using Monte Carlo simulations.

## II. THE PROPOSED LOAD FREQUENCY CONTROL SCHEME

The multi-area LFC maintains grid frequency of different areas within certain tolerance limits by controlling the generation rates and the power exchanges between them, as shown in Figure 1. The LFC also ensures the load sharing between the sub-systems, keeping the frequency deviation within limits. The area control error (ACE)<sub>*i*</sub> for each area *i* is generated as a weighted summation of the frequency deviation error ( $\Delta f$ )<sub>*i*</sub> and the tie-line power exchange ( $\Delta P_{Tie}$ ) between the two areas is kept to the minimum possible level using the controllers employed in the respective areas.

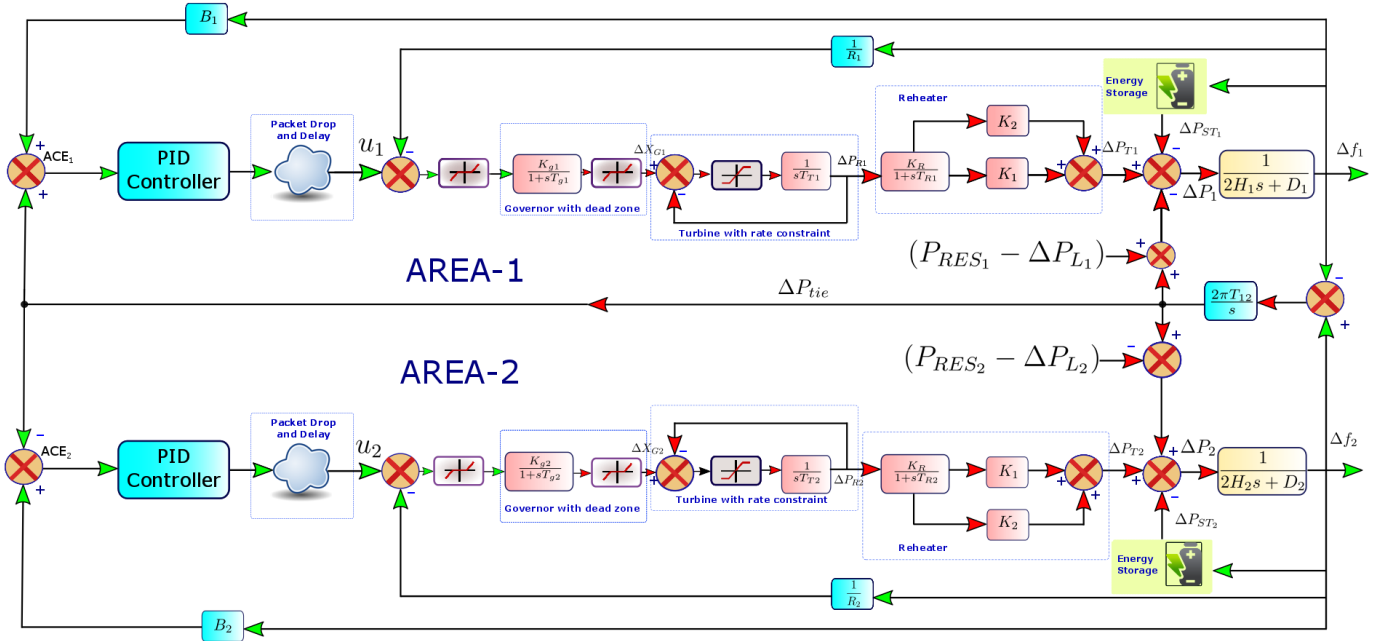


Figure 1: Schematic of the two-area LFC scheme with RES and energy storage with filtered PID controllers. The dead zones between the controller and governor increase the RES utilization in the smart grid.

Brief description of the models of the thermal power plant and energy storage devices are given below.

#### A. LFC in Conventional Fossil Fuel Power Plant Units

The thermal power plant model in each area consists of the steam governor with dead-zone, a steam turbine with the rate constraints and a reheater system, as shown in Figure 1. The first-order dynamic models, along with their associated nonlinearities, are modelled as per the scheme in [11]. The coefficients  $1/R_i$  in the  $i^{\text{th}}$  area are the primary control gain and the droop constant of the governor which act upon to reduce the immediate frequency fluctuations. The coefficients  $B_i$  act upon the longer fluctuations which act as a bias to the inter-area fluctuations. The PID controller used in the scheme in Figure 1 minimizes the area control error (ACE) comprising of the frequency deviations and the inter-area tie-line power oscillations. As given in [43], the frequency deviation due to load change in one area is not corrected by the controller in the other areas in case of primary frequency control. While in the secondary frequency control, the deviations due to the load changes are generally corrected using the tie-line power exchange between the two areas. This deviation is reflected in the system using  $(ACE)_i$  for each area  $i$  which is defined as:

$$ACE_i = \sum_{j=1}^M \Delta P_{ij} + B_i \Delta f_i, \quad (1)$$

where,  $\Delta P_{ij}$  represents tie-line power flow from the  $i^{\text{th}}$  area to the  $j^{\text{th}}$  area,  $\Delta f_i$  is the frequency deviation in the  $i^{\text{th}}$  area, and  $M$  is the number of areas connected to the  $i^{\text{th}}$  area. The bias factor due to frequency ( $B_i$ ) is generally expressed as a combination of speed regulation ( $R_i$ ) and damping coefficient ( $D_i$ ) which is given in (2) as:

$$B_i = (1/R_i) + D_i. \quad (2)$$

The nonlinearity in the system is represented by a generation rate constraint (GRC) and the dead zone for the governor and

the turbine, respectively. A reheater is also considered in the thermal power plant as a first-order model, which is shown in Figure 1. It increases the steam quality at the turbine exhaust and improves the thermodynamic efficiency of the power plant. Several realistic modelling aspects like nonlinearities, e.g. GRC in turbines in the LFC loops have been studied in [44], [45], dead-zone in [46] along with reheat turbine [47]. Due to the regulations to increase the usage of the RES, in the proposed scheme, the increase in the conventional thermal power plant outputs for each area  $i$  are only activated when the RES generation is unable to meet the increased load demand, with the control input  $\tilde{u}_i$  to the governor given as:

$$\tilde{u}_i = \max[\hat{u}_i - (\Delta f_i/R_i), 0], \quad (3)$$

where,  $\hat{u}_i$  signifies the controller output after the communication network with DoS attacks and random delays.

#### B. Nonlinear Models of Energy Storage Devices

The energy storage devices are connected to the grid as per the scheme in [41]. In [48], the stochastic nature of RES is incorporated in the battery energy operation instead of direct solar power output. However in this paper, first-order models for the energy storage elements are used viz. ultra-capacitors (UCs) [49], electric vehicles (EVs) [16], battery storage, flywheel [41], fuel cell (FC) and the solar power output is separately modelled so that the aggregated power of a bus is obtained. The energy storage devices have been used to damp out the grid frequency fluctuations due to load disturbances instead as a control device in [11]–[13], [25]. The detailed energy storage scheme used in Figure 1 is shown in Figure 2.

First-order model of the EVs has been used without any nonlinearity constraint [16]. The diesel generator has a rate constraint nonlinearity, but its operation is limited to restrain the harmful emissions from the fuel combustion. Hence it is scheduled to start only when the frequency deviations are

beyond 0.05 p.u. The GRCs for the energy storage components are given as  $|\dot{P}_{fw}| < 0.9$ ,  $|\dot{P}_{bat}| < 0.05$ ,  $|\dot{P}_{uc}| < 1.2$ ,  $|\dot{P}_{DG}| < 0.5$ ,  $|\dot{P}_{fc}| < 0.1$ . The rate constraints account for the electro-mechanical constraints of the storage devices. The overall dynamics of the storage devices are governed by the relative values of its gains and time constants. This property of energy storage devices influences the overall response of the LFC system as it consists of a combination of fast and slow dynamics of various components.

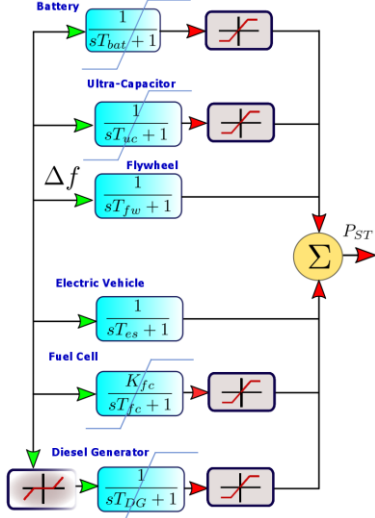


Figure 2: First order storage device models with nonlinearities like dead bands, output saturations and generation rate constraints.

### C. DoS Cyberattack and Stochastic Time Delay Models

In networked control system (NCS), packet drops and time delays are usually considered from sensor to controller and controller to actuator paths [50]. In the context of load frequency control, the feedback and the forward path is analogous to the data transmitted from the remote terminal units (RTU) to the control center and from control center to the generation companies where the governor set-point is transmitted. As given in [51], the application layer in the communication system is responsible for the transmission of data packets within a given bandwidth from the control center to the generation company (GENCO) which makes it vulnerable to DoS cyber-attack [52]. Time delay is considered due to the transmission of the data from the control center to the governor control system. The packet drops and delays are considered negligible in the feedback path and significant in the forward path.

The DoS attack in the form of random packet drops is modelled in cascade with a random time delay model, as addressed in [53]. The random time delay model considered here detains the PID controller output by random amount following a Gaussian distribution  $\tau_d \sim \mathcal{N}(\mu_d, \sigma_d^2)$ . The distribution parameters  $\mu_d$  and  $\sigma_d$  are considered as 1.5 and 0.1, respectively, for the simulation of random time delays.

Let us now consider the total time interval for consideration is  $T$  seconds. The packet transmission occurs when certain criteria, as in [32]–[34], is satisfied, which is given as:

$$P_{\text{Trans}} = \mathbb{P}(a_{\text{DoS}} > p_{\text{drop}}), \quad (4)$$

where,  $a_{\text{DoS}} \sim \mathcal{U}[0,1]$  is uniformly distributed and  $p_{\text{drop}}$  governs the packet transmission rate by regulating the number of packets to be dropped. The control packet is held over the interval till the next event (4) is satisfied, and the next packet is transmitted. The controller output after interrupted transmission of the packets can be modelled using the following logic. Let us consider the sampling time for the controller output be given as  $T_s$ , and the discrete-time instants are expressed as:

$$\zeta = \{0, 1, \dots, (N-1)T_s, NT_s\}, \quad (5)$$

where  $N = T/T_s$  and  $T$  represents total simulation time.

Now we consider the time instants  $\zeta_{\text{Trans}} \subset \zeta = \{t_0, \dots, t_N\}$  where (4) is satisfied and the control packets are transmitted. Here,  $N$  represents the time instants where (4) is satisfied. Let us consider  $\mathcal{H}$  be the Heaviside step function defined by:

$$\mathcal{H}(t) = \begin{cases} 1 & t \geq 0 \\ 0 & t < 0. \end{cases} \quad (6)$$

When the packets are not transmitted from the controller, the packet at previous instant goes to the actuator. Hence, we can model this using a zero-order hold (ZOH) which is represented using the difference between the Heaviside unit step function  $\mathcal{H}$  between two instants. We denote the delayed control signal as  $\hat{u}(t) = u(t - \tau_d)$ . Hence, the control output from the communication network can be expressed as:

$$\begin{aligned} \hat{u}_i(t) &= \hat{u}(t_0) + [\hat{u}(t_1) - \hat{u}(t_0)] \cdot \mathcal{H}(t_1 - t_0) \\ &\quad + [\hat{u}(t_2) - \hat{u}(t_1)] \cdot \mathcal{H}(t_2 - t_1) + \dots \\ &\quad + [\hat{u}(t_N) - \hat{u}(t_{N-1})] \cdot \mathcal{H}(t_N - t_{N-1}) \\ &= \hat{u}(t_0) + \sum_{i=1}^N [\hat{u}(t_i) - \hat{u}(t_{i-1})] \cdot \mathcal{H}(t_i - t_{i-1}). \end{aligned} \quad (7)$$

Here,  $\{t_0, \dots, t_N\} \in \zeta_{\text{Trans}}$  be the time instants when (4) is satisfied and  $i$  be the instant of the sample when the signal is transmitted. Substituting the value of  $\hat{u}_i(t)$  in equation (7), the governor input is represented as:

$$\begin{aligned} \tilde{u}_i(t) &= \max\{\hat{u}_i(t) - (\Delta f_i / R_i), 0\} \\ &= \max\left\{\hat{u}(t_0) + \sum_{i=1}^N [\hat{u}(t_i) - \hat{u}(t_{i-1})] \cdot \mathcal{H}(t_i - t_{i-1}) - (\Delta f_i / R_i), 0\right\}. \end{aligned} \quad (8)$$

As per (4), a higher  $p_{\text{drop}}$  makes  $P_{\text{Trans}}$  quite small, thus transmitting a lower number of packets inside the LFC loop. Furthermore, it reduces the value of  $N$  thus limiting the number of time instants in  $\zeta_{\text{Trans}}$ .

### D. Global Optimization based PID Controller Tuning

PID controllers with derivative filters are used in both the areas of the LFC loops to reduce the effect of noise and stochastic disturbances. The controllers are tuned considering the nonlinearities and stochasticity in the system due to random delays and cyberattack models. Previous studies in [53], [54] have shown that tuning PID controllers considering the upper limit of the stochastic delays and packet dropout probability rate

as an adversarial tuning method by including the stochastic cyberattack models in the tuning phase, helps to improve the control performances as compared to controller tuning using static lumped delay assumption without considering the intrinsic stochasticity in the system. Hence the value of  $p_{\text{drop}}$  considered to be 0.99 during the PID controller tuning phase. The load disturbances in the form of step inputs are unequal for the two areas and have been considered as active while tuning the PID controllers using constrained single objective global optimization. The controller is tuned by minimizing the Integral of Squared Error (ISE) criterion which aims to minimize sustained frequency fluctuations as compared to other time-weighted criteria like the integral of time multiplied squared error (ITSE). The former penalizes large oscillations as opposed to small sustained oscillations at a later time and helps to prevent the damage to the connected components to the grid. The weighted sum of the ACEs and the squared deviations of the control signals in two areas are considered as the objective function to be minimized for controller tuning as:

$$J = \sum_{i=1}^2 \int_0^{\infty} \left( w_1 (B_i \Delta f_i + \Delta P_{Tie})^2 + w_2 (\Delta u_i)^2 \right) dt$$

$$= \sum_{i=1}^2 \int_0^{\infty} \left( w_1 (\text{ACE}_i)^2 + w_2 (\Delta u_i)^2 \right) dt, \quad (9)$$

where,  $w_1 = w_2 = 0.5$  indicating equal weightage on both the objectives – ACE and the control effort and  $i$  represents each area. The four tuning parameters of the PID controller with the derivative filter i.e.  $\{K_p, K_i, K_d, N\}$  as shown in Figure 1 for each area, are tuned using the global optimizer PSO by minimizing the weighted objective function (9). PSO has been widely utilized for handling linear and nonlinear systems with optimal PID controllers in [55]–[57] where the performance of the tuned PID controllers are shown to be acceptable under various operating conditions. The research in [58], [59] requires the system to have dual loops for minimizing the energy consumption, thus keeping the parameters within a specific limit. However, in this study, an expected minimum of the stochastic objective function (9) is achieved using PSO, satisfying the given objectives. Our study shows that the system tends to be more stable when high communication packet drops and random time delays are considered in the tuning phase with PSO as an adversarial mechanism. Most of the earlier works have tuned controllers by optimizing static objective function without the stochastic components in such complex systems. Due to the presence of random packet drops for simulating DoS attack and stochastic delays in the NCS, the cost function also becomes stochastic, even for a deterministic step load disturbance in both the areas. Global optimization-based controller design approaches for such NCS problems have been previously studied in [53],[54],[60],[61]. These approaches of optimizing dynamic and stochastic objective function have been shown to outperform deterministic objective function-based controller design methods for NCS applications which have also been adopted in this paper.

The PSO algorithm consists of the swarm of particles  $x_i$   $\forall i \in \{1, 2, \dots, n_p\}$  where  $n_p$  is given by the user. The position and the velocity of each particle is updated in each

iteration as given by [62]:

$$x_i^{k+1} = x_i^k + v_i^{k+1},$$

$$v_i^{k+1} = \bar{\alpha} v_i^k + \bar{\beta}_1 \theta_{1,i}^k (x_i^{\text{best},k} - x_i^k) + \bar{\beta}_2 \theta_{2,i}^k (x_{\text{swarm}}^{\text{best},k} - x_i^k), \quad (10)$$

where,  $\bar{\alpha}$  represents the inertia factor,  $\bar{\beta}_1$  is the cognitive learning rate and  $\bar{\beta}_2$  is the social learning rate which influences the exploration and exploitation nature of the particles. The values  $\theta_{1,i}^k$  and  $\theta_{2,i}^k$  represent random numbers uniformly distributed in the interval  $\mathcal{U}[0,1]$ . The variable  $x_i^{\text{best},k}$  represents the previously obtained best value while  $x_{\text{swarm}}^{\text{best},k}$  denotes the best position of the swarm at iteration  $k$  and expressed as:

$$x_i^{\text{best},k} := \underset{x_i^j}{\text{argmin}} \{ f(x_i^j), 0 \leq j < k \},$$

$$x_{\text{swarm}}^{\text{best},k} := \underset{x_i^k}{\text{argmin}} \{ f(x_i^k), \forall i \}. \quad (11)$$

The PID controllers in the LFC system are tuned with a deterministic step load disturbance but random NCS components. The system with the designed controller is then tested against various stationary and nonstationary input profiles of load and RES for testing its robustness.

### III. MATHEMATICAL MODELS OF STOCHASTIC LOAD DEMANDS AND RES GENERATION PROFILES

The power produced due to solar and wind energy depends on the power electronic energy conversion devices, as shown in Figure 1 to integrate into the smart grid. The solar power needs a DC-DC converter interconnection and an inverter which has a time constant of  $T_{IN}$  and  $T_{I/C}$  respectively, as described in [63]. Since the induction generator dynamics of a wind generator is faster than the turbine, it is ignored, and the latter is considered as a first-order model using gain  $K_{\text{WTG}}$  and time constant  $T_{\text{WTG}}$ .

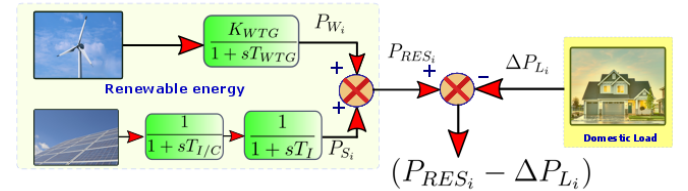


Figure 3: RES generation and load model used in the LFC scheme.

The uncertainty of the RES generation has been considered in different stochastic profiles used for modelling. The maximum solar and wind power output in each area is limited to 0.01 pu and 0.02 pu, respectively using appropriate bias and gain as analogous to the maximum rating of the solar and wind power installed in each area. The maximum load demand in area 1 is limited to 0.03 pu and 0.025 pu as analogous to the maximum demand contracted by the consumer with the utilities. The mathematical models of various stochastic input profiles are described in the next subsections.

### A. Filtered White Gaussian Noise (wGn) Profile

The system is tested considering the input profile as wGn as given in [26]. The generated white noise is filtered using a bandpass filter which yields a correlated noise. The transfer function of the bandpass filter used is given by:

$$\mathcal{B}_{bp}(s) = \frac{1}{1800s+1} + \frac{300s}{300s+1}. \quad (12)$$

The random number generated from the wGn generator which has equal intensities at all frequencies is represented by:

$$p_G(z) = \frac{1}{\sigma\sqrt{2\pi}} \exp\left(-\frac{(z-\mu)^2}{2\sigma^2}\right), \quad (13)$$

where,  $\mu$  represents the mean and  $\sigma$  represents the standard deviation of the signal. For this case, we assume,  $\mu=0$  and  $\sigma=1$ . The power generated in (13) is passed through the bandpass filter in (12) to produce a correlated noisy signal which is further conditioned to keep the load demand, solar power and wind power within the given bounds.

### B. Nonstationary Synthetic Input Profiles

The wind velocity and solar irradiation can be modelled using various other random number generators (RNGs) e.g. fractional Brownian motion [64]–[66] and geometric Brownian motion [67]–[69]. The wind speed needs to be modelled such that it represents the spatial dependencies of the wind flow. The power production due to wind is highly dependent on the fluctuation of the wind speed, especially at higher values due to the turbulent behaviour. The output of wind power varies with the wind velocity as [70]:

$$P_w(t) = \begin{cases} 130 - 63v(t) + 9.1v^2(t) - 0.3v^3(t) & ; 4 < v(t) < 15 \text{ m/s} \\ 140 + 11v(t) - 0.36v^2(t) & ; 15 \leq v(t) < 26 \text{ m/s} \\ 0 & ; v(t) > 26 \text{ m/s.} \end{cases} \quad (14)$$

Here,  $v(t)$  is considered as the stochastic variable and  $P_w(t)$  is the wind power generated due to the random variable  $v$  in (14). Similarly, for solar power, the solar irradiance  $\Phi$  is considered as the random variable, which is related to the production of solar PV power as given in [71]:

$$P_{pv} = \eta S \Phi(t) \{1 - 0.005(\mathbf{T}_a + 25)\}, \quad (15)$$

where, the parameter  $\eta=10\%$  is the conversion efficiency of the PV cells,  $S=4084 \text{ m}^2$  is the measured area of the PV array,  $\Phi$  is measured in  $\text{kW/m}^2$  which is the solar radiation of the PV cells and  $\mathbf{T}_a=25^\circ \text{C}$  is considered as the ambient temperature. The nonstationary signals used to model  $v(t)$  and  $\Phi(t)$  are given as the following two RNGs – fBm and gBm.

#### 1) Fractional Brownian Motion (fBm) Profile

The wind velocity has been modelled as an fBm in [66]. As given in [72], Brownian Motion is defined as  $\mathcal{B}$ , having the following properties:

- $\mathcal{B}_0 = 0$ ,
- For  $n \geq 1$  and  $0 < t_0 < t_1 < \dots < t_n$ , the increments  $\delta\mathcal{B}_{t_0 t_1}, \delta\mathcal{B}_{t_1 t_2}, \dots, \delta\mathcal{B}_{t_{n-1} t_n}$  are independent,

- For  $0 \leq \tilde{s} < t$  we have  $\delta\mathcal{B}_{\tilde{s} t} \sim \mathcal{N}(0, t - \tilde{s})$ .

For fractional Brownian motion, if  $\mathcal{B}(t)$  is the ordinary Brownian motion and  $H$  is the Hurst parameter satisfying  $0 < H < 1$  then, the fBm is defined as the moving average (MA) of Brownian motion  $\mathcal{B}(t)$ , in which past increments of

$\mathcal{B}(t)$  are weighted by  $(t - \tilde{s})^{H-1/2}$  [73]. Defining  $t$  as the time such that  $-\infty < t < \infty$  and  $\omega$  belonging to the samples space  $\Omega$ , one can write the Brownian motion as  $\mathcal{B}(t, \omega)$ . Hence random function  $\mathcal{B}_H(t, \omega)$  is defined considering  $\mathcal{b}_0$  as the arbitrary real number such that:

$$\begin{aligned} \mathcal{B}_H(0, \omega) &= \mathcal{b}_0 \\ \mathcal{B}_H(t, \omega) - \mathcal{B}_H(0, \omega) &= \frac{1}{\Gamma\left(H + \frac{1}{2}\right)} \left\{ \int_{-\infty}^0 \left[ (t - \tilde{s})^{H-1/2} - (-\tilde{s})^{H-1/2} \right] d\mathcal{B}(\tilde{s}, \omega) \right. \\ &\quad \left. + \int_0^t (t - \tilde{s})^{H-1/2} d\mathcal{B}(\tilde{s}, \omega) \right\}. \end{aligned} \quad (16)$$

For  $H=1/2$ ,  $\mathcal{B}_H(t, \omega)$  represents a Brownian motion. For

other value of  $H$ , it represents fractional derivative or integral of Brownian motion as defined in [74].  $\Gamma(\cdot)$  represents the Gamma function or generalized factorial. For  $H > 1/2$ , there is a positive autocorrelation and for  $H < 1/2$  there is a negative auto-correlation. The expectation of the function is given by:

$$\mathbb{E}[\mathcal{B}_H(t, \omega)\mathcal{B}_H(\tilde{s}, \omega)] = \frac{1}{2} (|t|^{2H} + |\tilde{s}|^{2H} - |t - \tilde{s}|^{2H}). \quad (17)$$

Solar irradiation is highly nonstationary; hence the analysis does not give the correct value of  $H$ , but better trends have been obtained using the detrended fluctuation analysis (DFA) in [65]. The Hurst exponent  $H=0.7$  is obtained for solar irradiation which proves that the signals have a persistent long-range correlation. Considering the homogeneous turbulence of the wind speed as given in [66], Hurst exponent  $H=1/3$  has been considered to model the wind speed. For area 1, the wind speed ( $v$ ) is considered from 4-15 m/s and in area 2, the wind speed is considered from 0-30 m/s. The wind and solar power are calculated from the wind speed and solar irradiation values from (14) and (15) respectively. The load demand fluctuations as the probabilistic forecast have been tackled in [64] using fBm, as it depends on the range and length of the Hurst exponent. Hence the value of  $H=0.185$  in this paper to model the randomness in load demand. The fBm has been simulated in MATLAB using the function  $\mathcal{fBm}()$  from the Wavelet Toolbox [75].

#### 2) Geometric Brownian Motion (gBm) Profile

Next, the stochastic process  $S_t$  is considered to follow a gBm as described in [76] if it satisfies the SDE defined as:

$$dS_t = \mu S_t dt + \sigma S_t d\mathcal{B}_t, \quad (18)$$

where,  $\mu$  is the percentage drift and  $\sigma$  represents the volatility rate where the former models the deterministic trends while the latter explains the unpredictability in the motion. Under Ito's representation, the SDE defined in (18) has the solution:

$$S_t = S_0 \exp\left(\left(\mu - \left(\sigma^2/2\right)\right)t + \sigma\mathcal{B}_t\right), \quad (19)$$

where,  $S_0$  is the initial condition. The nonstationary nature of the process is inferred from the expectation and covariance defined as:

$$\begin{aligned} \mathbb{E}[S_t] &= S_0 e^{\mu t}, \\ \text{Var}[S_t] &= \mathbb{E}[S_t - \mathbb{E}[S_t]]^2 = S_0^2 e^{2\mu t} (e^{\sigma^2 t} - 1). \end{aligned} \quad (20)$$

The distributed lag model has been used to predict the local levels of the incoming solar radiation in [69] where it was found that it follows a gBm. Time-varying rate parameter has been used to model the stochastic nature of the RES in [48]. However, as per [69], a constant value also captures the stochasticity of monthly solar irradiation variation. The rate ( $\mu = 0.014$ ) and the drift ( $\sigma^2 = 0.019$ ) are obtained from [69] to generate the random input profiles for solar irradiation. The solar PV power from the RNG is obtained from (15) using the gBm profile. The gBm has been simulated in MATLAB using the function `gBm()` in the Financial Toolbox [77].

The stochastic behaviour of the energy consumption and wind speed has been discussed in [67], [68] using Ornstein-Uhlenbeck (OU) Brownian motion model. The physical model is based on the motion of the particles of Brownian motion under friction, and it tends to drift towards its long-term mean. It is defined as the solution of the SDE ( $\boldsymbol{\chi}_t$ ) as:

$$d\boldsymbol{\chi}_t = -\theta\boldsymbol{\chi}_t dt + \sigma d\mathcal{B}_t, \quad (21)$$

where,  $\theta > 0$  and  $\sigma > 0$ .

Considering  $\boldsymbol{\chi}_0$  as constant, we can define the expectation and covariance as:

$$\begin{aligned} \mathbb{E}[\boldsymbol{\chi}_t] &= \boldsymbol{\chi}_0 e^{-\theta t} + \mu(1 - e^{-\theta t}), \\ \text{cov}(\boldsymbol{\chi}_{\bar{s}}, \boldsymbol{\chi}_t) &= \frac{\sigma^2}{2\theta} \left( e^{-\theta|t-\bar{s}|} - e^{-\theta(t+\bar{s})} \right). \end{aligned} \quad (22)$$

The SDE (21) is used to model the energy consumption of the multi-area power system in [68]. The OU gBm model has been used in continuous time to represent the wind speed as it models its long term daily cycle in [67], for energy system balancing. Numerical solution of the SDE is defined in [78]. Here, the OU process is defined as the univariate Markov process  $\boldsymbol{X}$  that evolves with time  $t$  as per the Langevin equation with its update formula given as:

$$\boldsymbol{X}(t + \Delta t) \approx \boldsymbol{X}(t) - \frac{1}{\tau} \boldsymbol{X}(t) \Delta t + c^{1/2} \boldsymbol{\nu}(\Delta t)^{1/2}, \quad (23)$$

where,  $\boldsymbol{\nu}$  represents the sample value of the unit normal random variable  $\mathcal{N}(0,1)$ ,  $\tau$  represents relaxation time and  $c$  represents diffusion constant. Based on the Langevin equation, the constants  $\tau$  and  $c$  can be defined to represent the parameters of the SDE defined as:

$$\tau = 1/\theta, c = \sigma^2. \quad (24)$$

The values of  $\{\theta, \sigma\}$  for the load demand and wind velocity are obtained in [67], [68]. The wind velocity is converted into equivalent wind power using the model in (14).

### C. Real Datasets as the Input Profiles

Beside synthetic profiles as described above, real data is used from the Dalrymple ESCRI battery energy project [79] where the load demand, solar irradiation and wind power values are obtained at 4-sec, 1 min and 4-sec interval respectively. One-month data has been used for our analysis. The per-second values are generated using a higher-order interpolation algorithm `interp1()` in Matlab with modified Akima method as described in [80], although other interpolators could have been used as well. After the data is read and partitioned as per 5 mins interval, it is conditioned (by adjusting the gain and bias) so that the output value is within the given prescribed limits. Randomly selected 1000 samples (out of ~8350) are used in the simulations. The solar power is obtained from the solar irradiance values using (15). Since in the real data, for some instants, the solar and wind power are not available, care has been taken that the data is normalized and cleaned before using in the LFC simulations.

## IV. RESULTS AND DISCUSSIONS

### A. PID Controller Tuning for LFC as Global Optimization

The PSO algorithm, as described in Section II.D, is used to minimize the stochastic objective function in (9) for tuning the two PID controllers simultaneously through a random search and optimization process. Simulations were run on a Windows PC Intel Xeon E5-2687W CPU, 3 GHz processor with 12 parallel cores. The LFC model in Simulink is run with the `ode8()` Dormand Prince solver with a fixed step size of 0.1 sec.

The default recommended values  $\bar{\alpha}, \bar{\beta}_1, \bar{\beta}_2, \theta_{1,i}^k, \theta_{2,i}^k$  has been considered in the PSO algorithm as in [81], using the function `particleswarm()` from the Global Optimization Toolbox in MATLAB [82]. Objective function tolerance value of  $10^{-6}$  has been used for convergence of the PSO algorithm. The search range for the three controller gains is  $\{K_p, K_i, K_d\}_i \in \mathcal{U}[-1, 1]$

for both the areas and the filter constants  $N_i \in \mathcal{U}[0, 1]$ , using 80 particles to navigate the 8D controller parameter space for both the areas. The search ranges were limited to ensure faster convergence of the optimizer. The optimum PID controller parameters are obtained considering a 0.01 pu step load change in area 1 and a 0.02 pu step load change in area 2. Tuning both areas with different magnitude of step input makes the LFC scheme more robust to other disturbances. The PSO algorithm has been run 10 times independently with the convergence characteristics shown in Figure 4, with the best solution found in each iteration from a stack of all datapoints visited in the random search process. It is observed that in some cases the PSO algorithm converges quickly, while in some others, it converges after a larger number of iterations which is due to the high complexity of the proposed LFC with NCS considerations. The best controller parameters for the LFC system is considered in the run, which yielded the lowest objective function value. Average time for convergence of the 10 PSO runs is 3500 seconds  $\approx$  58.33 minutes, as shown in Figure 4.

The objective function values traversed by the particles in the successive PSO iterations are stacked together to visualize the exploration characteristics. Moreover, in the search process, the

feasible or stabilizable region are also obtained in the controller parameter space [83]. The  $J_{\text{best}}$  obtained from  $x_{\text{swarm}}^{\text{best,k}}$  is plotted in Figure 5. It shows the pairwise approximate bivariate distribution of the objective function as a function of the PID controller parameters in both the areas. The sampled data points shown in Figure 5 correspond to a threshold of  $J_{\text{best}} < 0.01$ . The colorbar represents the objective function values which converge towards the expected global minima of the stochastic objective function. The graph shows a nonconvex pattern revealing the need of meta-heuristic optimization and the trajectory of the particles moving towards the expected minima after randomly navigating the objective function space. We observe a thicker blue patch for area 1 as compared to area 2, which suggests that the particles moved towards the minima faster in area 1 as compared to area 2, which can be primarily accounted due to smaller magnitude of the load disturbance in area 1 as compared to in area 2. The exploration of the particles in the joint controller parameter space is shown in Figure 6. It reveals the stabilizable region in the controller parameter space. The cluster of particles around the optima is thicker for area 1 as compared to the one in area 2, which indicates that the convergence for area 2 is slower than area 1.

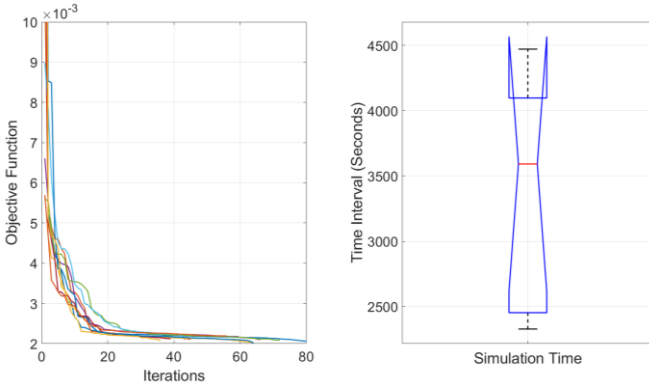


Figure 4: (left) 10 independent simulation runs of PSO and its convergence characteristics, (right) total time taken for PSO to converge.

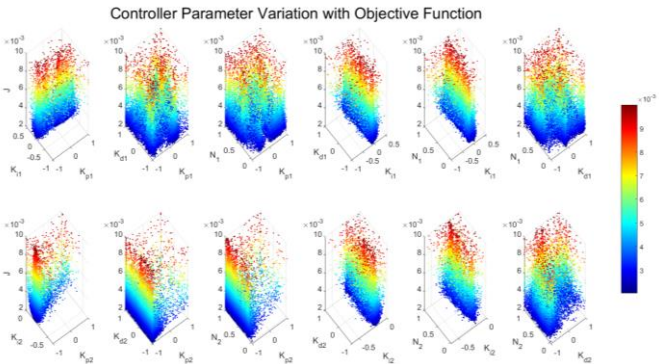


Figure 5: Convergence/bivariate distribution of the objective functions in terms of the PID controller parameters; (top panels) area 1, (bottom panels) area 2.

### B. Testing with Deterministic Change in Load Demand

Deterministic step inputs of 0.01 pu and 0.02 pu are now applied in two areas, and the responses are analyzed. Since the parameters in the NCS like  $\alpha_{\text{DoS}}$  and  $\tau_d$  are sampled from the respective stochastic processes, the grid frequency fluctuations are analyzed considering 100 Monte Carlo system simulations and shown in Figure 7 for three different packet dropout levels. The controller tuning was done considering 99% packet drop

probability. The maximum frequency fluctuations  $(\Delta f_i)_{\text{max}}$  obtained in our case are lesser than as it was obtained in benchmarks results by Nanda *et al.* [84] and also for similar step load responses, albeit being tested on a much complex LFC model. The response is also better than the complex LFC model considering the time delay in [31] with a PID controller. Our results are also better in terms of maximum deviation  $(\Delta f_i)_{\text{max}}$  for the LFC problem with time delays reported in [27], [28], [30] where  $(\Delta f_i)_{\text{max}}$  is  $5 \times 10^{-3}$ ,  $5 \times 10^{-3}$  and 0.1 pu, respectively. Similarly, event-triggered problems with cyber-attack for LFC solved in [32], [33], [35] have  $(\Delta f_i)_{\text{max}}$  as 0.05, 0.06 and 0.04 pu respectively. Combination of cyber-attack and time delay was studied in [39], which resulted  $(\Delta f_i)_{\text{max}}$  as  $2 \times 10^{-5}$  pu, but the time delay ( $\tau$ ) was considered to be quite small. The cyber-attack considered in [39] is limited by frequency and time duration, unlike this paper, where a much higher packet drop rate is considered.

Moreover, previous analyses were conducted mostly on simpler LFC models without considering any nonlinearities in the energy storage components. The control performance is superior in our work as compared to these because they mostly used some variants of convex optimizers like linear matrix inequalities (LMIs), semi-definite programming on simpler linear LFC models. These methods can ensure guaranteed convergence to global optima, considering the objective function being convex. However, in the present work, the models contain significant nonlinearities along with stochastic network induced delays and packet drops which makes the problem nonconvex. These realistic effects make the optimization problem intractable using the traditional convex optimization algorithms. It is better solved by meta-heuristic global optimizers involving nonconvex multi-agent search like PSO, which gives an improved performance.

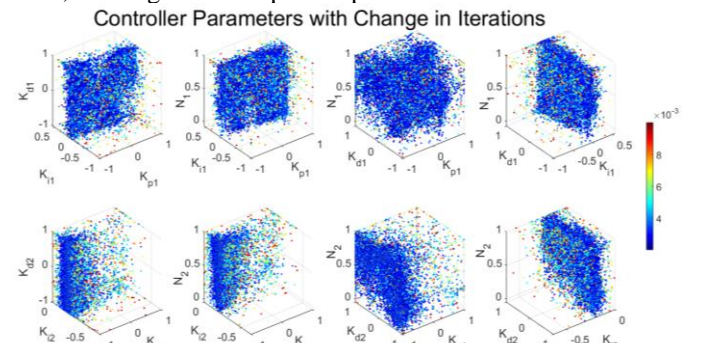


Figure 6: Multivariate distribution or feasible/stabilizable region in the PID controller parameters  $\{K_p, K_i, K_d, N\}$ . Colorbar represents ISE values.

The oscillations in the grid frequency can be compared to the results reported in [29] where the controller was tuned using computational intelligence techniques for a complex LFC with similar load changes in both the areas. The stochastic simulations conducted for different cases of packet drops and random delays are shown in Figure 8 and Figure 9. It is evident in Figure 8 that since the controller was tuned for 99% packet drop, the control input moving towards the steady-state value even though only fewer packets are successfully transmitted. However, when the packet transmission rate is even lower, the delayed control signal starts oscillating. The control signals



transmitted at an average 0.5% rate makes it oscillatory. However, when the packet transmission rate is reduced to 0.1%, the delayed control signals get unbounded and makes the LFC system unstable. Hence, we observe that with sparse packet transmission, control inputs work on a lesser amount of discrete levels exposing the system with a higher switch in control input magnitude. The effect of the control signal at several discrete levels is seen in Figure 8 and Figure 9. Figure 8 shows the comparison of having and not having random delays in the NCS as the delay makes the control signal larger and more oscillatory.

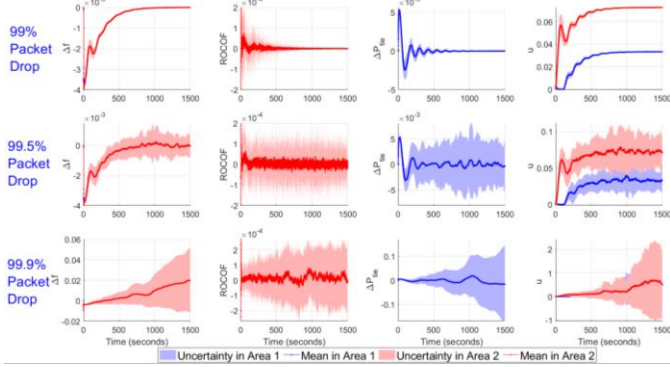


Figure 7: Step response of proposed LFC with 99%, 99.5% and 99.9% packet drops as the DoS attack on both the areas with 100 Monte Carlo simulations.

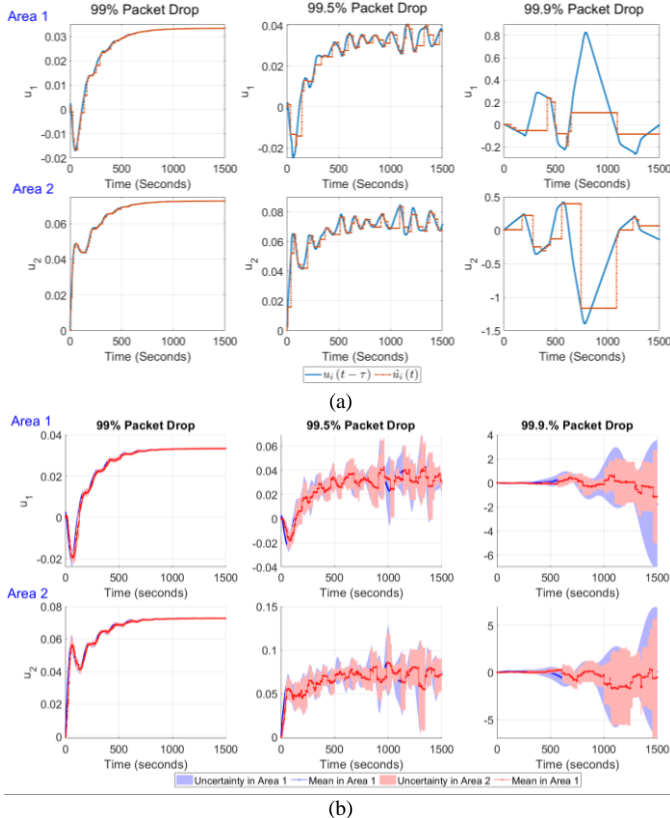


Figure 8: (a) Simulations of the delay-free and randomly delayed control signal for two areas with 99%, 99.5% and 99.9% packet drop. (b) Simulations of the delayed control signal for two areas with 99%, 99.5% and 99.9% packet drop.

Since the system was tuned with 1% packet transmission, the system is stable with the fluctuations being relatively small. The tie-line power fluctuations also quickly settle to steady-state

values after the initial oscillations. The effect of stochasticity imposed by the imperfect communication networks is also small in case of 1% packet transmission, as we see a small deviation band between the ensemble runs. However, when  $p_{\text{drop}}$  is increased to 99.5%, the stochastic nature of the NCS becomes predominant, creating a more considerable fluctuation in the frequency, thus causing oscillations in tie-line power. The higher deviation between the simulated ensembles is also observed, which is mainly because the control packet is working at higher discrete levels, as seen in Figure 8. When  $p_{\text{drop}}$  is increased to 99.9%, the time instants of transmission decreases, which furthermore reduces  $N$ . Under these NCS settings, the oscillatory behaviour of the LFC system increases, making the system unstable.

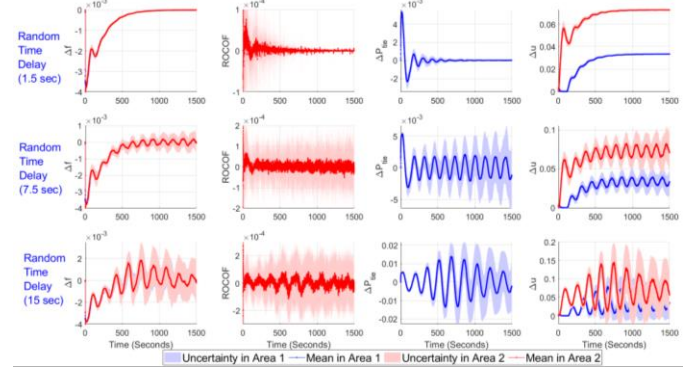


Figure 9: Step response of the LFC with  $\mu_d = 1.5$  seconds, 7.5 second and 15 seconds of random delay with 100 Monte Carlo runs.

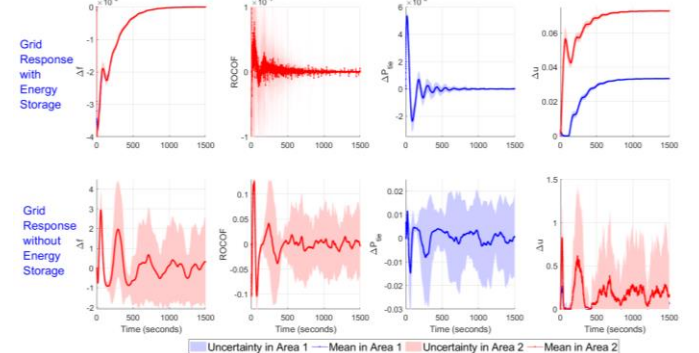


Figure 10: Step response of the system with and without energy storage elements with 100 Monte Carlo runs.

A similar effect is also visible by increasing the value of  $\mu_d$  in the random time delay ( $\tau_d$ ) samples in the simulation. An increase in the magnitude of the grid frequency and tie-line power is observed with the increase in  $\mu_d$ . Even though  $\mu_d$  is increased 10 times with the nominal controller parameters, it increases the oscillations of the systems, but it does not make the system to be unstable, unlike reduction in packet transmission rates. It confirms the fact that in an LFC problem as an NCS, the DoS cyberattack in the form of a high rate of packet losses are much more detrimental than simpler random communication delays. Energy storage devices play an essential role in keeping the frequency fluctuations within specified limits and shown in Figure 10. The LFC system will undergo higher fluctuations without the presence of energy storage elements. The frequency and the ROCOF fluctuations obtained without energy storage in Figure 10 are unacceptable

and might cause the relays in the protective system to trip, hence affecting the grid operation. Thus, while integrating stochastic RES generation profiles, it is essential to tune the LFC system with energy storage elements.

C. Testing with Stochastic RES and Load Demand Profiles

The LFC system with the PID controller parameters obtained has now been tested against stochastic profiles which has been defined in Section III after 100 Monte Carlo simulation runs on a Windows PC with Intel Core i5-8500 CPU, 3 GHz processor with 6 parallel cores. However, due to the complexity of the system, it becomes computationally intensive to run the Monte Carlo runs. The computation breaks down if the memory is not cleared after subsequent runs. The LFC model in Simulink was numerically integrated with `ode8()` Dormand-Prince solver with a fixed step size of 0.01 seconds. The simulation was run for 300 seconds, thus generating 30000 samples per run. The memory was subsequently cleared after running the simulation 10 times, thus improving the computing performance of the algorithm. The input solar power generation and load demand profiles are generated based on 100 Monte Carlo simulations of the models as described before. The input files are generated in a batch of 10 Monte Carlo iterations and automatically saved, in order to reduce the memory overload of the PC while testing. The input profiles, as shown in Figure 11, is generated by reading each of these stored files. The variations in the wind power input profiles in the case of fBm and gBm for different areas are due to the consideration of the different range of wind speeds in the respective areas. The ROCOF fluctuations are calculated as per 0.1-sec interval as per the IEEE standards [42]. It is evident from Figure 12, Figure 13, Figure 14 and Figure 15 that the frequency fluctuations and the ROCOF are within the prescribed limits for connecting the RES to the smart grid [42] for different RNGs as filtered Gaussian, fBm, gBm and real data respectively.

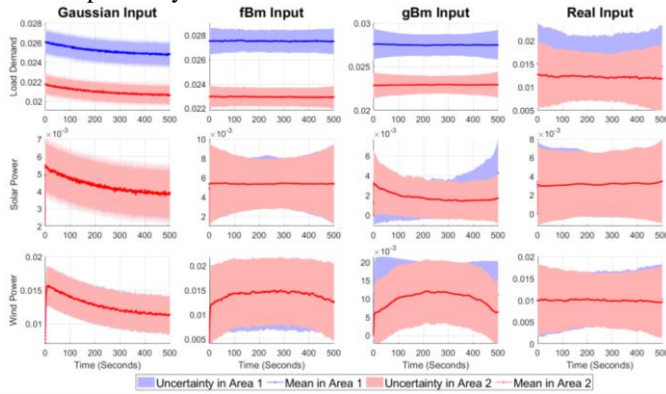


Figure 11: Stochastic input, real RES and load demand profiles for the smart grid LFC with the 100 Monte Carlo runs.

The standard for over-frequency (OF) and under-frequency (UF) trips are defined as 1.2 and 1.5 Hz (for 60 Hz grid) which turns out to be 0.02 and 0.025 pu respectively. It is evident from our results that the maximum fluctuations  $(\Delta f_i)_{\max}$  are 0.0015 pu in the case of filtered Gaussian inputs, 0.004 pu in case of fBm and gBm input profile and 0.0035 for real data set which are much below the prescribed limit, hence showing the efficacy of the designed LFC system for future smart grids with NCS considerations. The results obtained is also better than the

$(\Delta f_i)_{\max}$  obtained in [11], [25], [21], [22], [23], [24], [26] where this value lies in the range of 0.02, 0.1, 0.01, 0.02, 0.2 and 0.025 pu respectively where the LFC contains stochastic RES models.

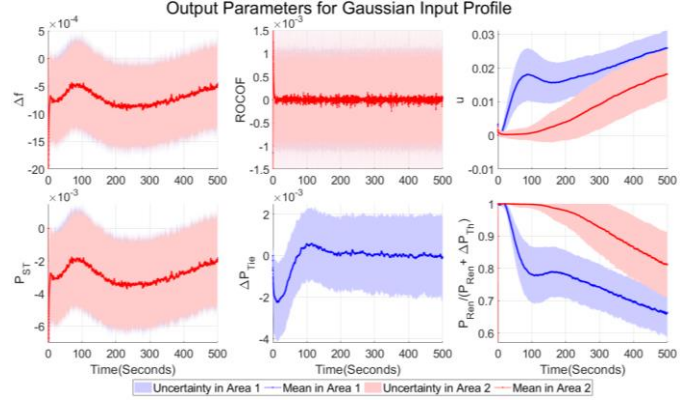


Figure 12: Smart grid performance indicators for Gaussian input profile: (top left) frequency deviation, (top center) rate of change of frequency, (top right) control input to the thermal power plant, (bottom left) energy storage output, (bottom center) tie-line power between two areas, (bottom right), proportion of renewable energy usage for the 100 Monte Carlo runs.

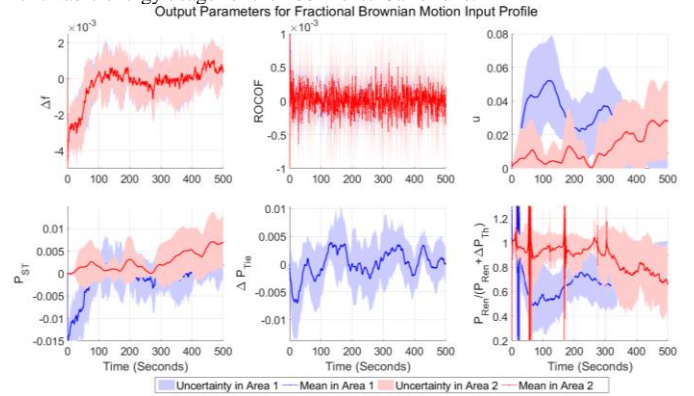


Figure 13: Smart grid performance indicators for fBm input profile: (top left) frequency deviation, (top center) rate of change of frequency, (top right) control input to the thermal power plant, (bottom left) energy storage output, (bottom center) tie-line power between two areas, (bottom right), proportion of renewable energy usage for the 100 Monte Carlo runs.

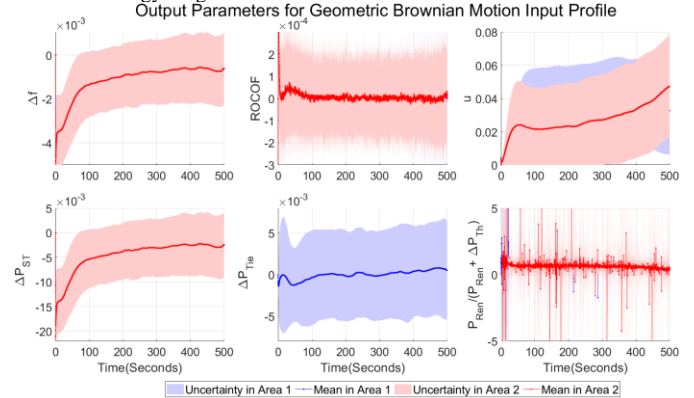


Figure 14: Smart grid performance indicators for gBm input profile (top left) frequency deviation, (top center) rate of change of frequency, (top right) control input to the thermal power plant, (bottom left) energy storage output, (bottom center) tie-line power between two areas, (bottom right) proportion of renewable energy usage for the 100 Monte Carlo runs.

The ROCOF for the IEEE standard is given as 0.5 Hz/sec (for 60 Hz grid), considering the minimum specifications in [42] which are calculated as 0.008 pu. We see in Figure 12, Figure 13, Figure 14 and Figure 15 that the maximum ROCOF are

within 0.002 pu in the case of Gaussian input, 0.0005 pu in the case of fBm input, 0.003 pu in the case of gBm input and real input profile, which is bounded within the prescribed standards, showing the strength of our LFC design as a NCS.

The thermal power generation reduction against these profiles are analyzed along with the frequency deviation in both the areas. In order to monitor the utility of the proposed LFC scheme, we calculate a custom parameter as the ratio between the renewable power generation and the total generation using both the renewable and thermal units as:

$$PP_{\text{ren}} = (100 \times P_{\text{ren}}) / (\Delta P_{\text{th}} + P_{\text{ren}}), \quad (25)$$

where,  $\Delta P_{\text{th}}$  represents a change in thermal power plant output meeting the stochastic load demand and  $P_{\text{ren}}$  represents the power generated by RES. We have now analyzed the results based on the values of  $PP_{\text{ren}}$ :

Case 1:  $PP_{\text{ren}} < 0$

$$\Rightarrow (\Delta P_{\text{th}} + P_{\text{ren}}) < 0 \Rightarrow \Delta P_{\text{th}} < 0 \text{ since } P_{\text{ren}} \geq 0,$$

Case 2:  $0 < PP_{\text{ren}} < 1$

$$\Rightarrow 0 < P_{\text{ren}} < (\Delta P_{\text{th}} + P_{\text{ren}}) \Rightarrow \Delta P_{\text{th}} > 0 \text{ since } P_{\text{ren}} \geq 0,$$

Case 3:  $PP_{\text{ren}} > 1$

$$\Rightarrow P_{\text{ren}} > (\Delta P_{\text{th}} + P_{\text{ren}}) \Rightarrow \Delta P_{\text{th}} < 0 \text{ since } P_{\text{ren}} \geq 0. \quad (26)$$

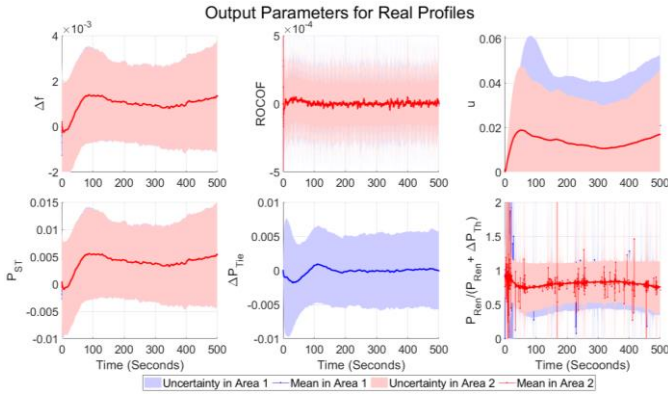


Figure 15: Smart grid performance indicators for real input profile (top left) frequency deviation, (top centre) rate of change of frequency, (top right) control input to the thermal power plant, (bottom left) energy storage output, (bottom centre) tie-line power between two areas (bottom right) proportion of renewable energy usage for the 100 Monte Carlo runs.

We observe from Figure 14, the value of the  $PP_{\text{ren}} > 1$  for some time instants, hence  $\{\Delta P_{\text{th}}\}_i < 0$ , for real power profile. It suggests that there is a reduction in the thermal power plant output. Similar trends are also observed for system response for fBm and gBm inputs in Figure 13 and Figure 14, especially in the latter case where the maximum value of  $PP_{\text{ren}}$  goes beyond  $\pm 5$  suggesting that there is a considerable reduction in thermal power plant output  $\{\Delta P_{\text{th}}\}_i$ . The control inputs to the actuators are also calculated as (3) which is constrained to be positive which ensure that the thermal power plants are always operated to meet the base-load demand but otherwise will maintain a minimum constant firing rate or increase the firing when the RES and storage elements together are incapable of meeting the increase in load demand.

We can analyze the operation from the energy balance

model. Since RES and thermal power plant produce power, we can write the expression of total power generated  $(P_{\text{Gen}})_i$  for each area  $i$  as:

$$\text{Power Generated } (P_{\text{Gen}})_i = (P_{\text{ren}} + \Delta P_{\text{th}})_i. \quad (27)$$

Considering energy storage devices as power-consuming devices, we can write the total power consumed as:

$$\text{Power Consumer } (P_{\text{Con}})_i = (P_{ST} + \Delta P_L)_i. \quad (28)$$

Since the frequency fluctuations due to renewable energy sources are within limits, we can consider the energy balance condition is met. Hence from (27) and (28) we can write:

$$\begin{aligned} (P_{\text{ren}} + \Delta P_{\text{th}})_i &\approx (P_{ST} + \Delta P_L)_i \\ \Rightarrow \{\Delta P_{\text{th}}\}_i &\approx \{P_{ST} + \Delta P_L - P_{\text{ren}}\}_i. \end{aligned} \quad (29)$$

Since for fBm, gBm and real input profiles  $PP_{\text{ren}} > 1$ , it is apparent that  $\{\Delta P_{\text{th}}\}_i < 0$ . Thus we can infer from (29):

$$\{P_{ST} + \Delta P_L - P_{\text{ren}}\}_i < 0 \Rightarrow \{P_{ST}\}_i < \{P_{\text{ren}} - \Delta P_L\}_i. \quad (30)$$

This means that the energy storage charging rate is not high enough to absorb the excess power generated by the renewable energy source. Hence thermal power plant output has to be reduced at some time instants. However, the value of  $PP_{\text{ren}}$  is between (0,1), as shown in Figure 12 when the RES and load are modelled by a Gaussian profile, which suggests that thermal power plant output is  $\{\Delta P_{\text{th}}\}_i > 0$ , which can be analyzed using the relation in (29) as:

$$\{P_{ST} + \Delta P_L - P_{\text{ren}}\}_i > 0 \Rightarrow \{P_{ST}\}_i > \{P_{\text{ren}} - \Delta P_L\}_i \quad (31)$$

As per the relation in (31), the discharging dynamics of energy storage elements are not fast enough to meet the load. Hence thermal power plant output is positive in the case of Gaussian input profiles. We also observe a common trend in these simulations that the fluctuations in energy storage outputs  $\{P_{ST}\}_i$  is similar to the frequency fluctuation of the grid. Similar patterns are observed in the control signals to the thermal power plant, as shown in all the 4 stochastic input profile. The tie-line power exchange of nonstationary profiles like fBm and gBm are similar to the real input profile as compared to the Gaussian input profile. The similarity of the profiles can be ascertained more strongly in the next section by considering the norms of the frequency fluctuations and tie-line power and multivariate statistical analyses of the grid parameters.

#### D. Hypothesis Testing Using the Datasets of Frequencies of Each Area and the Tie-Line Power Fluctuations

The norms of the simulated signals  $\{\Delta f_1, \Delta f_2, \Delta P_{tie}\}$  from the LFC system are calculated next, considering the samples after 10 sec which discards the initial transient behavior of the solar and wind power generation systems due to filtered RNGs. The  $p$ -norm of a real valued signal  $\bar{x} = \{\bar{x}_1, \dots, \bar{x}_n\}$  is given as:

$$\|\bar{x}\|_p := \left( \sum_{i=1}^n |\bar{x}_i|^p \right)^{1/p}. \quad (32)$$

For  $p=1$ , the  $\|\bar{x}\|_1$  represents the projection of the signal  $\bar{x}$  on the coordinate axis. For  $p=2$ ,  $\|\bar{x}\|_2$  represents the Euclidean distance of the signal  $\bar{x}$  from the origin. In the case of  $\Delta f$ ,  $L_1$ -norm and  $L_2$ -norm represent the absolute deviation and squared deviation from the ideal value.

The  $L_\infty$ -norm of the signals are defined as:

$$\|\bar{x}\|_\infty := \max(|\bar{x}_1|, \dots, |\bar{x}_n|). \quad (33)$$

It represents the maximum value of a signal along its length. In the case of  $\{\Delta f\}_i$ , it is defined as the maximum deviation from the ideal value. The frequency fluctuations are now visualized by a scatter plot between their  $L_1$ ,  $L_2$ ,  $L_\infty$ -norms of the signals, obtained from the Monte Carlo runs, as shown in Figure 16.

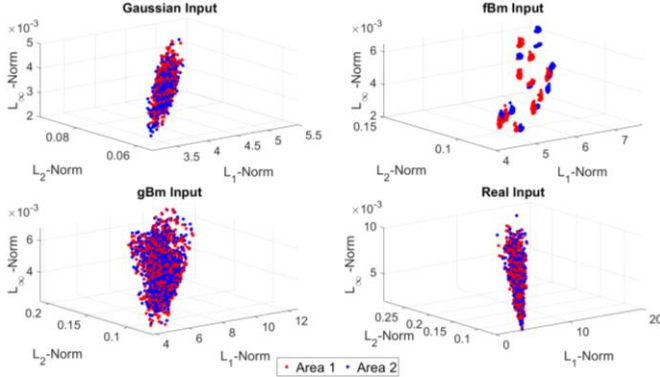


Figure 16: Scatter-plots of the  $L_1$ ,  $L_2$  and  $L_\infty$  norms of the frequency fluctuations with different RNGs: (left top) Gaussian inputs, (left-right) fBm inputs, (left bottom) gBm inputs, (right bottom) real inputs.

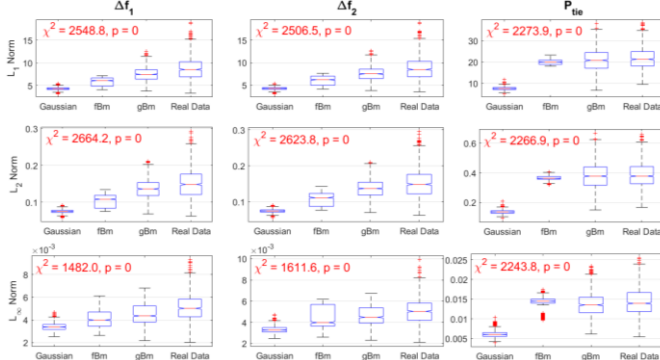


Figure 17: Box-plots of the  $L_1$ ,  $L_2$  and  $L_\infty$  norms of the frequency fluctuations in the two areas and tie-line power exchange for different input profiles. The  $p$ -values are also reported for each case using the Kruskal-Wallis test.

We can observe from Figure 16 that the frequency fluctuation is highest and lowest in the case of real and Gaussian input profiles, respectively, which is evident from the  $L_1$  and  $L_\infty$  norm axes. Lower fluctuation in the  $L_1$  and  $L_\infty$  norm plots in the case of Gaussian input profile can be attributed due to the value of  $PP_{ren}$  between 0 and 1 thus making the  $\Delta P_{th} > 0$  whose dynamics are slower than the RES, hence damping out the fluctuations. Higher  $L_1$  and  $L_\infty$  norm in case of real input profiles can be attributed due to solar/wind power being zero at particular time instants since the power plant outputs have to deal with the stochastic nature of the load profiles. Range of variation of different norms are similar in case of fBm and gBm input profiles, but few small island formations are seen in the signal norms for the former case, which is because  $\{\Delta f\}_i$  has high-frequency components in case of fBm profile as compared

to gBm. These differences in the pattern can be attributed due to higher complexity captured by the Hurst exponent  $H$  in the input profile, causing wilder fluctuations.

The hypothesis test is conducted on the  $L_1$ ,  $L_2$ ,  $L_\infty$ -norms of the frequency fluctuation signals  $\{\Delta f\}_i$  and tie-line power fluctuation  $\Delta P_{tie}$ , as obtained from the Monte Carlo runs for different stochastic generation and demand profiles as shown in Figure 16. The similarity in the system operation for different stochastic profiles can be analyzed by comparing the respective  $p$ -values and  $\chi^2$ -values obtained from the nonparametric Kruskal-Wallis hypothesis testing, as shown in the boxplots Figure 17. In order to decide whether to perform a parametric or nonparametric test on the processed data (and derived signal norms), it is necessary to check their univariate normality. The univariate normality checks are conducted using the Anderson-Darling, Kolmogorov-Smirnov [85] and Lilliefors test [86] where the significance levels of all tests are kept at 0.01. The tests are conducted using the functions `adtest()`, `kstest()` and `lillietest()` from the Statistics and Machine Learning Toolbox in MATLAB.

As given in the supplementary material, some of the signal norms usually are distributed while in some other cases, they are not, but the joint normality of all the input profiles (Gaussian, fBm, gBm, real data) are not encountered anywhere. Hence, the parametric version – analysis of variance (ANOVA) test cannot be performed on these samples. Instead, the nonparametric version - Kruskal Wallis test [87] needs to be used to compare the medians of these four different input profiles. This test has been performed using the null hypothesis that all the 4 cases come from the same distribution, against the alternative hypothesis that they do not. The  $p$ -values and  $\chi^2$  values are obtained using the function `kruskalwallis()` from the Statistics and Machine Learning Toolbox in MATLAB, which compares the medians of the samples. The  $\chi^2$ -values defined for the tests are defined as the critical values, and the  $p$ -values are defined as the probability that the test statistic is more than the critical value. The  $p$ -values are found to be zero, suggests that the norms of the input profiles do not follow a similar distribution. The  $\chi^2$ -values are smaller for  $L_\infty$  norm as compared to  $\chi^2$ -values for  $L_1$  and  $L_2$  norms which suggests that maximum fluctuation is greater than the sum of absolute and square of the fluctuations of  $\{\Delta f_1, \Delta f_2, \Delta P_{tie}\}$  around zero due to the stochastic nature of the input fluctuation. It makes the frequency and tie-line powers hover around zero, but the PID controller for the thermal power plant will keep them maximum fluctuation within limits.

The  $L_\infty$ -norms in case of frequency fluctuations are smallest in the case of Gaussian input profile, as compared to other profiles, which is primarily due to higher active operation of the thermal power plant  $\Delta P_{th} > 0$ . The frequency fluctuations for fBm and gBm input signals are similar to the fluctuations in the case of real input profiles. These nonstationary profiles capture the behaviour of real input profiles more accurately and show a higher utilization of the RES since  $\Delta P_{th} < 0$ . The fluctuation of gBm input profiles resembles more to the real input data.

Similar conclusions are also valid for the tie-line power  $\Delta P_{Tie}$  between two areas except in the case of fBm where the variance is smaller than its other nonstationary counterparts. The small variance in the tie-line power within the ensembles can also be considered for the reason behind the small island formation in Figure 16. The norms for the tie-line power is similar for the gBm input profile as compared to the real input profile.

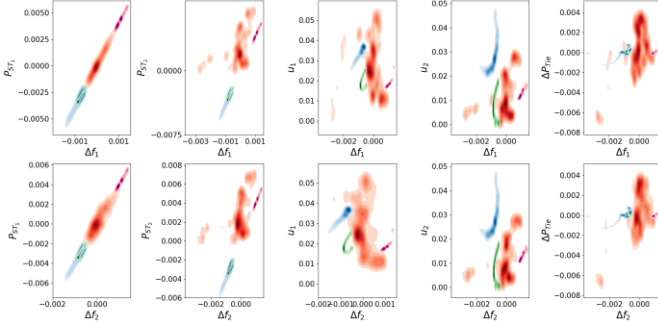


Figure 18: Multivariate KDE plots of the grid parameters with the frequency fluctuations in each area. The colors represent different RNGs: red = fBm, green = Gaussian, blue = gBm, magenta = real data.

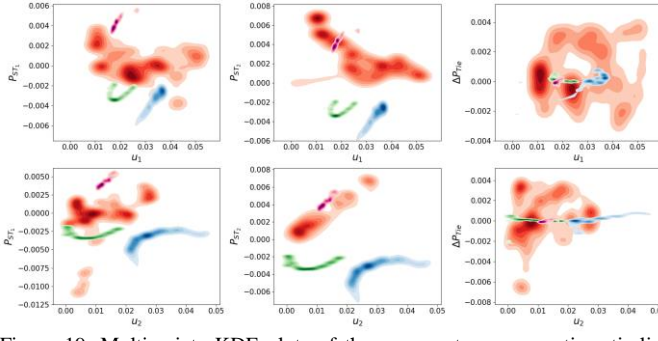


Figure 19: Multivariate KDE plots of the energy storage operation, tie-line power with the control input to the governor in two areas. The colors represent different RNGs: red = fBm, green = Gaussian, blue = gBm, magenta = real data.

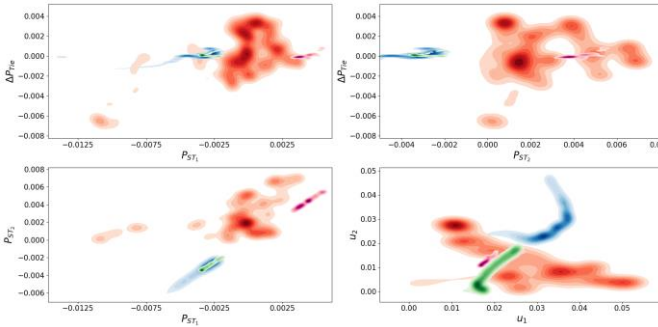


Figure 20: Multivariate KDE plot of (a) Tie-line power and storage operation in area 1 (top-left) (b) Tie-line power and storage operation in area 2 (top-right) (c) Storage operation in both the areas (bottom-left) (d) Control input for both the areas (bottom-right). The colors represent different RNGs: red = fBm, green = Gaussian, blue = gBm, magenta = real data.

### E. Multivariate Analysis of Grid Performance Measures

Multivariate kernel density estimate (KDE) plots are shown in Figure 18, Figure 19 and Figure 20, using the mean of the ensembles generated from the Monte Carlo simulations. There is a high correlation between the energy storage operation in both the areas and frequency fluctuations as shown in Figure 18, which suggests that they play a crucial role in damping out the frequency fluctuations in the grid. The mean profile suggests that the energy storage devices work in discharge mode in case of real and normal input, and charge mode in case

of gBm input, and both the modes in the case of fBm input. The higher control input to the governor is required to damp out the frequency fluctuations in area 1 in case of fBm input profile while control input is highest in area 2 for gBm input profile. We also observe a correlation between the control inputs in both the areas for normal and real input profile. High correlation is also observed between the storage operation in the two areas. The grid parameters show unusual behaviour when the input profile is fBm with higher fluctuation in the mean curve, thus creating an unusual spread in the multivariate plots and signifying low correlation amongst themselves which also explains the formation of the islands in the norm plots in Figure 16.

## V. CONCLUSIONS

We demonstrate here the effect of packet dropouts and delays to the controller output posed by the communication network to the LFC loop. The LFC loop is designed in such a way to promote the usage of RES to mitigate the stochastic load demand. The system response is checked using the controller, which is tuned using the PSO algorithm. The LFC system response is checked with step-input and varying levels of communication transmission dropouts and delay. The tuned LFC system with delay and dropout is tested with stochastic renewable generation inputs and load demand profiles on the grid performance parameters. The system analysis is conducted using 100 Monte Carlo simulations from various stochastic input profiles, and the results are benchmarked with real input dataset. The data analysis is conducted to check the usage of RES in the control loop and its effect on the various frequency and tie-line power fluctuation measures.

The main findings from our simulation studies are:

- PSO serves as an efficient optimizer for maintaining control performance of the LFC loops with interrupted packet transmission as DoS cyberattacks and random delays.
- The frequency fluctuations ( $\Delta f$ ) and the ROCOF are within the prescribed limits, as per the IEEE standard [42] for all the four stochastic input profiles – Gaussian, fBm, gBm, and real data.
- The renewable energy usage in the case of nonstationary profiles like fBm and gBm is similar to the real input profiles, where the LFC tends to decrease the thermal power plant output  $\{\Delta P_{th} < 0\}_i$ . However, the opposite trend is observed in the case of Gaussian input where  $\{\Delta P_{th} > 0\}_i$ . Hence frequency and tie-line power fluctuations are smaller in the case of Gaussian input. Hence, the variability in the norms obtained from the real input profile is highest and in the case of Gaussian input profiles, it is the lowest.
- The response of the LFC in the smart grid is more similar to real data in case of nonstationary profiles than the stationary profiles.
- High correlation is obtained for the frequency response in both areas. The correlation is also visible in the frequency fluctuations and energy storage operation in LFC, thus

signifying that the latter plays an essential role in damping out the frequency fluctuations.

Future work can be directed towards testing the LFC system with other complex controller structures and also studying the nature of frequency and tie-line power fluctuations to gain deeper insights about the system operations. The LFC with RES and battery storage can also be validated on larger grid models. The packet drop is considered to be a high-frequency signal. Hence its location in the feedback path causes it to produce filtered noise from the controller. Hence the results here cannot be generalized to interrupted data transmission at different control paths. This issue will be addressed in future papers.

#### APPENDIX

**Parameters for Area 1:**  $T_g=0.08$  sec,  $T_i=0.4$ sec,  $R=3$ ,  $D=0.015$ ,  $2H=0.1667$ ,  $B=0.3483$ ,  $T_{12}=0.2$ ,

**Parameters for Area 2:**  $T_g=0.06$  sec,  $T_i=0.44$ sec,  $R=2.73$ ,  $D=0.016$ ,  $2H=0.2017$ ,  $B=0.3827$ ,  $T_{21}=0.2$ ,

**Storage Parameters:**  $T_{uc}=0.1$  sec,  $T_{es}=1$  sec,  $T_{fw}=0.1$  sec,  $T_{bat}=0.1$  sec,  $T_{dg}=0.3$  sec,  $T_{ic}=4$  sec,  $K_{fc}=0.01$ ,

**Solar Parameters:**  $T_{IN}=0.04$  sec,  $T_{1C}=0.004$  sec,

**Wind Parameters:**  $K_{WTG}=1$ ,  $T_{WTG}=1.5$  sec.

Univariate normality tests for the synthetic and real input profiles are provided in the supplementary materials using three different hypothesis tests. High resolution images are also provided in the supplementary material.

#### REFERENCES

- [1] I. G. Mason, S. Page, and A. Williamson, "A 100% renewable electricity generation system for New Zealand utilising hydro, wind, geothermal and biomass resources," *Energy Policy*, vol. 38, no. 8, pp. 3973–3984, 2010.
- [2] E. Pursiheimo, H. Holtinen, and T. Koljonen, "Path toward 100% renewable energy future and feasibility of power-to-gas technology in Nordic countries," *IET Renewable Power Generation*, vol. 11, no. 13, pp. 1695–1706, 2017.
- [3] B. Römer, K. Aldonza, Y. Julliard, and O. Lewis, "Planning 100% renewable energy islands: The case of the Caribbean island of Montserrat," *CIREN-Open Access Proceedings Journal*, vol. 2017, no. 1, pp. 2488–2492, 2017.
- [4] B. Cosic, G. Krajavcic, and N. Duic, "A 100% renewable energy system in the year 2050: The case of Macedonia," *Energy*, vol. 48, no. 1, pp. 80–87, 2012.
- [5] D. Connolly and B. V. Mathiesen, "A technical and economic analysis of one potential pathway to a 100% renewable energy system," *International Journal of Sustainable Energy Planning and Management*, vol. 1, pp. 7–28, 2014.
- [6] H. Lund and B. V. Mathiesen, "Energy system analysis of 100% renewable energy systems—The case of Denmark in years 2030 and 2050," *Energy*, vol. 34, no. 5, pp. 524–531, 2009.
- [7] D. Connolly, H. Lund, B. V. Mathiesen, and M. Leahy, "The first step towards a 100% renewable energy-system for Ireland," *Applied Energy*, vol. 88, no. 2, pp. 502–507, 2011.
- [8] M. Esteban, Q. Zhang, and A. Utama, "Estimation of the energy storage requirement of a future 100% renewable energy system in Japan," *Energy Policy*, vol. 47, pp. 22–31, 2012.
- [9] M. Z. Jacobson, M. A. Delucchi, G. Bazouin, Z. A. Bauer, C. C. Heavey, E. Fisher, S. B. Morris, D. J. Piekutowski, T. A. Vencill, and T. W. Yeskoo, "100% clean and renewable wind, water, and sunlight (WWS) all-sector energy roadmaps for the 50 United States," *Energy & Environmental Science*, vol. 8, no. 7, pp. 2093–2117, 2015.
- [10] M. J. Alexander, P. James, and N. Richardson, "Energy storage against interconnection as a balancing mechanism for a 100% renewable UK electricity grid," *IET Renewable Power Generation*, vol. 9, no. 2, pp. 131–141, 2014.
- [11] I. Pan and S. Das, "Fractional-order load-frequency control of interconnected power systems using chaotic multi-objective optimization," *Applied Soft Computing*, vol. 29, pp. 328–344, 2015.
- [12] I. Pan and S. Das, "Kriging based surrogate modeling for fractional order control of microgrids," *IEEE Transactions on Smart Grid*, vol. 6, no. 1, pp. 36–44, 2014.
- [13] I. Pan and S. Das, "Fractional order fuzzy control of hybrid power system with renewable generation using chaotic PSO," *ISA Transactions*, vol. 62, pp. 19–29, 2016.
- [14] M.-H. Khooban, "Secondary load frequency control of time-delay standalone microgrids with electric vehicles," *IEEE Transactions on Industrial Electronics*, vol. 65, no. 9, pp. 7416–7422, 2017.
- [15] X. Qi, Y. Bai, H. Luo, Y. Zhang, G. Zhou, and Z. Wei, "Fully-distributed Load Frequency Control Strategy in an Islanded Microgrid Considering Plug-In Electric Vehicles," *Energies*, vol. 11, no. 6, p. 1613, 2018.
- [16] A. Safari, F. Babaei, and M. Farrokhifar, "A load frequency control using a PSO-based ANN for micro-grids in the presence of electric vehicles," *International Journal of Ambient Energy*, pp. 1–13, 2019.
- [17] H. R. Baghaee, M. Mirsalim, G. B. Gharehpetian, and H. A. Talebi, "A decentralized robust mixed  $H_2/H_\infty$  voltage control scheme to improve small/large-signal stability and ftr capability of islanded multi-der microgrid considering load disturbances," *IEEE Systems Journal*, vol. 12, no. 3, pp. 2610–2621, 2017.
- [18] V. Gholamrezaie, M. G. Dozein, H. Monsef, and B. Wu, "An optimal frequency control method through a dynamic load frequency control (LFC) model incorporating wind farm," *IEEE Systems Journal*, vol. 12, no. 1, pp. 392–401, 2017.
- [19] Z. Civelek, G. Gorel, M. Luy, N. Barisci, and E. Cam, "Effects on Load-Frequency Control of a Solar Power System with a Two-Area Interconnected Thermal Power Plant and its Control with a New BFA Algorithm," *Elektronika ir Elektrotechnika*, vol. 24, no. 6, pp. 3–10, 2018.
- [20] N. Sa-ngawong and I. Ngamroo, "Intelligent photovoltaic farms for robust frequency stabilization in multi-area interconnected power system based on PSO-based optimal Sugeno fuzzy logic control," *Renewable Energy*, vol. 74, pp. 555–567, 2015.
- [21] Z. Li, X. Li, and B. Cui, "Planar clouds based load frequency control in interconnected power system with renewable energy," *IEEE Access*, vol. 6, pp. 36459–36468, 2018.
- [22] Z. Yan and Y. Xu, "Data-driven load frequency control for stochastic power systems: A deep reinforcement learning method with continuous action search," *IEEE Transactions on Power Systems*, vol. 34, no. 2, pp. 1653–1656, 2018.
- [23] D. Ganger, J. Zhang, and V. Vittal, "Forecast-based anticipatory frequency control in power systems," *IEEE Transactions on Power Systems*, vol. 33, no. 1, pp. 1004–1012, 2017.
- [24] A. M. Prostejovsky, M. Marinelli, M. Rezkalla, M. H. Syed, and E. Guillo-Sansano, "Tuningless load frequency control through active engagement of distributed resources," *IEEE Transactions on Power Systems*, vol. 33, no. 3, pp. 2929–2939, 2017.
- [25] I. Pan and S. Das, "Fractional order AGC for distributed energy resources using robust optimization," *IEEE Transactions on Smart Grid*, vol. 7, no. 5, pp. 2175–2186, 2015.
- [26] J. Pahasa and I. Ngamroo, "Coordinated control of wind turbine blade pitch angle and PHEVs using MPCs for load frequency control of microgrid," *IEEE Systems Journal*, vol. 10, no. 1, pp. 97–105, 2014.
- [27] C. J. Ramlal, A. Singh, S. Rocke, and M. Sutherland, "Decentralized Fuzzy  $H_\infty$  Iterative Learning LFC With Time-Varying Communication Delays and Parametric Uncertainties," *IEEE Transactions on Power Systems*, vol. 34, no. 6, pp. 4718–4727, 2019.
- [28] A. Azarbahram, A. Amini, and M. Sojoodi, "Resilient fixed-order distributed dynamic output feedback load frequency control design for interconnected multi-area power systems," *IEEE/CAA Journal of Automatica Sinica*, vol. 6, no. 5, pp. 1139–1151, 2019.
- [29] M. Heshmati, R. Noroozian, S. Jalilzadeh, and H. Shayeghi, "Optimal design of CDM controller to frequency control of a realistic power system equipped with storage devices using grasshopper optimization algorithm," *ISA Transactions*, vol. 97, pp. 202–215, 2020.
- [30] A. D. Rosaline and U. Somarajan, "Structured H-Infinity Controller for an Uncertain Deregulated Power System," *IEEE Transactions on Industry Applications*, vol. 55, no. 1, pp. 892–906, 2018.
- [31] J. Sharma, Y. V. Hote, and R. Prasad, "PID controller design for interval load frequency control system with communication time delay," *Control Engineering Practice*, vol. 89, pp. 154–168, 2019.

- [32] X. Zhou, Z. Gu, and F. Yang, "Resilient event-triggered output feedback control for load frequency control systems subject to cyber attacks," *IEEE Access*, vol. 7, pp. 58951–58958, 2019.
- [33] J. Liu, Y. Gu, L. Zha, Y. Liu, and J. Cao, "Event-Triggered  $H_\infty$  Load Frequency Control for Multi-Area Power Systems Under Hybrid Cyber Attacks," *IEEE Transactions on Systems, Man, and Cybernetics: Systems*, vol. 49, no. 8, pp. 1665–1678, 2019.
- [34] C. Peng, J. Li, and M. Fei, "Resilient Event-Triggering  $H_\infty$  Load Frequency Control for Multi-Area Power Systems With Energy-Limited DoS Attacks," *IEEE Transactions on Power Systems*, vol. 32, no. 5, pp. 4110–4118, 2016.
- [35] Y. Li, P. Zhang, and L. Ma, "Denial of service attack and defense method on load frequency control system," *Journal of the Franklin Institute*, vol. 356, no. 15, pp. 8625–8645, 2019.
- [36] H. Yuan, Y. Xia, H. Yang, and Y. Yuan, "Resilient control for wireless networked control systems under DoS attack via a hierarchical game," *International Journal of Robust and Nonlinear Control*, vol. 28, no. 15, pp. 4604–4623, 2018.
- [37] A. Sargolzaei, K. K. Yen, M. N. Abdelghani, S. Sargolzaei, and B. Carburnar, "Resilient design of networked control systems under time delay switch attacks, application in smart grid," *IEEE Access*, vol. 5, pp. 15901–15912, 2017.
- [38] Z. Cheng, D. Yue, S. Hu, X. Xie, and C. Huang, "Detection-based weighted  $H_\infty$  LFC for multi-area power systems under DoS attacks," *IET Control Theory & Applications*, vol. 13, no. 12, pp. 1909–1919, 2019.
- [39] Z. Cheng, D. Yue, S. Hu, C. Huang, C. Dou, and L. Chen, "Resilient load frequency control design: DoS attacks against additional control loop," *International Journal of Electrical Power & Energy Systems*, vol. 115, p. 105496, 2020.
- [40] M. Olsson, M. Perninge, and L. Söder, "Modeling real-time balancing power demands in wind power systems using stochastic differential equations," *Electric Power Systems Research*, vol. 80, no. 8, pp. 966–974, 2010.
- [41] M.-H. Khooban, T. Dragicevic, F. Blaabjerg, and M. Delimar, "Shipboard microgrids: A novel approach to load frequency control," *IEEE Transactions on Sustainable Energy*, vol. 9, no. 2, pp. 843–852, 2017.
- [42] *IEEE Standard for Interconnection and Interoperability of Distributed Energy Resources with Associated Electric Power Systems Interfaces*, pp. 1547–2018, 2018.
- [43] M. I. Alomoush, "Load frequency control and automatic generation control using fractional-order controllers," *Electrical Engineering*, vol. 91, no. 7, pp. 357–368, 2010.
- [44] K. Sabahi, M. Teshnehlab, and others, "Recurrent fuzzy neural network by using feedback error learning approaches for LFC in interconnected power system," *Energy Conversion and Management*, vol. 50, no. 4, pp. 938–946, 2009.
- [45] K. Sudha and R. V. Santhi, "Robust decentralized load frequency control of interconnected power system with generation rate constraint using type-2 fuzzy approach," *International Journal of Electrical Power & Energy Systems*, vol. 33, no. 3, pp. 699–707, 2011.
- [46] T. Mohamed, H. Bevrani, A. Hassan, and T. Hiyama, "Decentralized model predictive based load frequency control in an interconnected power system," *Energy Conversion and Management*, vol. 52, no. 2, pp. 1208–1214, 2011.
- [47] S. A. Taher, M. H. Fini, and S. F. Aliabadi, "Fractional order PID controller design for LFC in electric power systems using imperialist competitive algorithm," *Ain Shams Engineering Journal*, vol. 5, no. 1, pp. 121–135, 2014.
- [48] J. Leithon, S. Sun, and T. J. Lim, "Demand response and renewable energy management using continuous-time optimization," *IEEE Transactions on Sustainable Energy*, vol. 9, no. 2, pp. 991–1000, 2017.
- [49] H. Li, X. Wang, and J. Xiao, "Differential evolution-based load frequency robust control for micro-grids with energy storage systems," *Energies*, vol. 11, no. 7, p. 1686, 2018.
- [50] W. Zhang, M. S. Branicky, and S. M. Phillips, "Stability of networked control systems," *IEEE Control Systems Magazine*, vol. 21, no. 1, pp. 84–99, 2001.
- [51] F. F. Wu, K. Moslehi, and A. Bose, "Power system control centers: Past, present, and future," *Proceedings of the IEEE*, vol. 93, no. 11, pp. 1890–1908, 2005.
- [52] Y. Xie and S.-Z. Yu, "Monitoring the application-layer DDoS attacks for popular websites," *IEEE/ACM Transactions on Networking*, vol. 17, no. 1, pp. 15–25, 2008.
- [53] I. Pan, S. Das, and A. Gupta, "Handling packet dropouts and random delays for unstable delayed processes in NCS by optimal tuning of  $PID^D$  controllers with evolutionary algorithms," *ISA Transactions*, vol. 50, no. 4, pp. 557–572, 2011.
- [54] I. Pan, S. Das, and A. Gupta, "Tuning of an optimal fuzzy PID controller with stochastic algorithms for networked control systems with random time delay," *ISA Transactions*, vol. 50, no. 1, pp. 28–36, 2011.
- [55] W.-D. Chang and S.-P. Shih, "PID controller design of nonlinear systems using an improved particle swarm optimization approach," *Communications in Nonlinear Science and Numerical Simulation*, vol. 15, no. 11, pp. 3632–3639, 2010.
- [56] T.-H. Kim, I. Maruta, and T. Sugie, "Robust PID controller tuning based on the constrained particle swarm optimization," *Automatica*, vol. 44, no. 4, pp. 1104–1110, 2008.
- [57] Z.-L. Gaing, "A particle swarm optimization approach for optimum design of PID controller in AVR system," *IEEE Transactions on Energy Conversion*, vol. 19, no. 2, pp. 384–391, 2004.
- [58] C. Yin, S. Wu, S. Zhou, J. Cao, X. Huang, and Y. Cheng, "Design and stability analysis of multivariate extremum seeking with Newton method," *Journal of the Franklin Institute*, vol. 355, no. 4, pp. 1559–1578, 2018.
- [59] C. Yin, S. Dadras, X. Huang, Y. Chen, and S. Zhong, "Optimizing Energy Consumption for Lighting Control System via Multivariate Extremum Seeking Control With Diminishing Dither Signal," *IEEE Transactions on Automation Science and Engineering*, vol. 16, no. 4, pp. 1848–1859, 2019.
- [60] I. Pan and S. Das, "Design of hybrid regrouping PSO-GA based sub-optimal networked control system with random packet losses," *Memetic Computing*, vol. 5, no. 2, pp. 141–153, 2013.
- [61] S. Das, S. Das, and I. Pan, "Multi-objective optimization framework for networked predictive controller design," *ISA Transactions*, vol. 52, no. 1, pp. 56–77, 2013.
- [62] R. Eberhart and J. Kennedy, "Particle swarm optimization," in *Proceedings of the IEEE International Conference on Neural Networks*, 1995, vol. 4, pp. 1942–1948.
- [63] H. Bevrani, F. Habibi, P. Babahajyani, M. Watanabe, and Y. Mitani, "Intelligent frequency control in an AC microgrid: Online PSO-based fuzzy tuning approach," *IEEE Transactions on Smart Grid*, vol. 3, no. 4, pp. 1935–1944, 2012.
- [64] J. L. T. Garcia, E. C. Calderón, E. R. Heras, and C. M. Ontiveros, "Generating electrical demand time series applying SRA technique to complement NAR and sARIMA models," *Energy Efficiency*, pp. 1–19, 2019.
- [65] M. Rypdal and K. Rypdal, "Is there long-range memory in solar activity on timescales shorter than the sunspot period?," *Journal of Geophysical Research: Space Physics*, vol. 117, no. A4, 2012.
- [66] R. Calif and F. G. Schmitt, "Modeling of atmospheric wind speed sequence using a lognormal continuous stochastic equation," *Journal of Wind Engineering and Industrial Aerodynamics*, vol. 109, pp. 1–8, 2012.
- [67] A. Loukatou, S. Howell, P. Johnson, and P. Duck, "Stochastic wind speed modelling for estimation of expected wind power output," *Applied Energy*, vol. 228, pp. 1328–1340, 2018.
- [68] M. Perninge, V. Knazkins, M. Amelin, and L. Söder, "Modeling the electric power consumption in a multi-area system," *European Transactions on Electrical Power*, vol. 21, no. 1, pp. 413–423, 2011.
- [69] S. S. Hamlen, W. A. Hamlen Jr, and J. T. Tschirhart, "Geometric Brownian distribution of solar radiation with an economic application," *Solar Energy*, vol. 21, no. 6, pp. 469–475, 1978.
- [70] E. Bossanyi, T. Burton, D. Sharpe, and N. Jenkins, "Wind energy handbook," 2000.
- [71] D.-J. Lee and L. Wang, "Small-signal stability analysis of an autonomous hybrid renewable energy power generation/energy storage system part I: Time-domain simulations," *IEEE Transactions on Energy Conversion*, vol. 23, no. 1, pp. 311–320, 2008.
- [72] I. Karatzas and S. E. Shreve, "Brownian motion," in *Brownian Motion and Stochastic Calculus*, Springer, 1998, pp. 47–127.
- [73] B. B. Mandelbrot and J. W. Van Ness, "Fractional Brownian motions, fractional noises and applications," *SIAM Review*, vol. 10, no. 4, pp. 422–437, 1968.
- [74] I. M. Gelfand and G. E. Shilov, *Generalized functions, Vol. 4: Applications of Harmonic Analysis*. Academic Press, 1964.
- [75] "Wavelet Toolbox." [Online]. Available: <https://uk.mathworks.com/products/wavelet.html>.

- [76] D. Dufresne, "The integral of geometric Brownian motion," *Advances in Applied Probability*, vol. 33, no. 1, pp. 223–241, 2001.
- [77] "Financial Toolbox." [Online]. Available: <https://www.mathworks.com/products/finance.html>.
- [78] D. T. Gillespie, "Exact numerical simulation of the Ornstein-Uhlenbeck process and its integral," *Physical Review E*, vol. 54, no. 2, p. 2084, 1996.
- [79] "DALRYMPLE ESCRI-SA BATTERY PROJECT." [Online]. Available: <https://www.escri-sa.com.au/>. [Accessed: 17-May-2019].
- [80] J. Fried and S. Zietz, "Curve fitting by Spline and Akima methods: possibility of interpolation error and its suppression," *Physics in Medicine & Biology*, vol. 18, no. 4, p. 550, 1973.
- [81] M. E. H. Pedersen, "Good parameters for particle swarm optimization," *Hvass Lab., Copenhagen, Denmark, Tech. Rep. HLI001*, pp. 1551–3203, 2010.
- [82] "Global Optimization Toolbox Matlab." [Online]. Available: <https://uk.mathworks.com/products/global-optimization.html>.
- [83] S. Das, K. Halder, and A. Gupta, "Delay Handling Method in Dominant Pole Placement based PID Controller Design," *IEEE Transactions on Industrial Informatics*, vol. 16, no. 2, pp. 980–991, 2020.
- [84] J. Nanda, S. Mishra, and L. C. Saikia, "Maiden application of bacterial foraging-based optimization technique in multiarea automatic generation control," *IEEE Transactions on Power Systems*, vol. 24, no. 2, pp. 602–609, 2009.
- [85] F. J. Massey Jr, "The Kolmogorov-Smirnov test for goodness of fit," *Journal of the American Statistical Association*, vol. 46, no. 253, pp. 68–78, 1951.
- [86] H. Abdi and P. Molin, "Lilliefors/Van Soest's test of normality," *Encyclopedia of Measurement and Statistics*, pp. 540–544, 2007.
- [87] P. E. McKight and J. Najab, "Kruskal-wallis test," *The Corsini Encyclopedia of Psychology*, pp. 1–1, 2010.



**Stuart Townley** received the B.Sc. in Mathematics and the PhD in Engineering from the University of Warwick, UK, in 1983 and 1987, respectively. He followed then with Postdoctoral positions at the University of Warwick and the University of Bath, UK. He joined the University of Exeter, Exeter, UK in 1990 as a Lecturer and he became a Professor of Applied Mathematics in 1999. Prof Townley has published more than 100 papers and his research interests range from fundamental theory to societal applications and span operator theory, mathematical analysis, adaptive and robust control, industrial applied mathematics, energy engineering, neural networks, e-Health, mathematical biology, evolution, population and conservation ecology.



**Deepak Kumar Panda** received BE in Power Engineering from Jadavpur University, India and M.Tech in Electrical Engineering from National Institute of Technology, Calicut, India in 2014 and 2016 respectively. He worked as an engineer in Schneider Electric during 2016-2018. He is currently pursuing PhD in the Department of Mathematics, University of Exeter, UK on data science and networked control of smart grids.



**Saptarshi Das** (M'19) received BE and ME in Power Engineering and PhD in Engineering all from Jadavpur University, India in 2007, 2010 and 2013 respectively. He worked in ALSTOM Projects India Ltd. during 2007-2008. During 2012-2015, he was a Post-doctoral Research Fellow at the School of Electronics and Computer Science, University of Southampton, UK and during 2015-2017, he was a Post-doctoral Research Associate at the Cavendish Astrophysics Group, Department of Physics, University of Cambridge, UK. Since 2017, he is a Lecturer in the Department of Mathematics, University of Exeter, Penryn Campus, UK. He has co-authored 2 books and more than 100 research papers in refereed scientific journals, conferences, and book chapters. His present research interests include dynamical systems and control theory, big data analytics, machine learning, computational intelligence, signal processing, and fractional calculus in diverse applications in energy, environment, and biomedical engineering.



# Supplementary Material

Table 1: Univariate Normality Tests for the Norms of the Grid Parameters for Different Input Profiles using 3 Different Distribution Tests

Signal norms	Grid parameters	Input Profile	Anderson Darling Test				Kolmogorov Smirnov Test				Lilliefors Test			
			h	p	Test Statistic	Critical Value	h	p	Test Statistic	Critical Value	h	p	Test Statistic	Critical Value
$L_1$ Norm	$\Delta f_1$	Gaussian	1	0.0005	37.817	1.033	1	0	0.99998	0.051	1	0.001	0.1732	0.033283294
		FBM	0	0.01217	0.9986	1.033	1	0	0.99933	0.051	0	0.0474	0.0288	0.033283294
		gBm	1	0.00255	1.2748	1.033	1	0	0.99992	0.051	0	0.0583	0.0281	0.033283294
		Real	1	0.0005	5.6454	1.033	1	0	0.99954	0.051	1	0.001	0.0484	0.033283294
	$\Delta f_2$	Gaussian	1	0.0005	23.509	1.033	1	0	0.99998	0.051	1	0.001	0.1379	0.033283294
		FBM	1	0.0005	2.05	1.033	1	0	0.9991	0.051	1	0.004	0.0357	0.033283294
		gBm	1	0.00212	1.3071	1.033	1	0	0.99993	0.051	0	0.0431	0.029	0.033283294
		Real	1	0.0005	5.5028	1.033	1	0	0.9998	0.051	1	0.001	0.0479	0.033283294
	$\Delta P_{ie}$	Gaussian	1	0.0005	18.446	1.033	1	0	1	0.051	1	0.001	0.1218	0.033283294
		FBM	1	0.00068	1.5081	1.033	1	0	1	0.051	0	0.0308	0.0301	0.033283294
		gBm	1	0.00298	1.2468	1.033	1	0	1	0.051	1	0.0082	0.0338	0.033283294
		Real	1	0.0005	3.595	1.033	1	0	1	0.051	1	0.001	0.0452	0.033283294
$L_2$ Norm	$\Delta f_1$	Gaussian	1	0.0005	24.328	1.033	1	8.13E-246	0.52994	0.051	1	0.001	0.1422	0.033283294
		FBM	1	0.00126	1.3996	1.033	1	1.15E-239	0.52326	0.051	1	0.0069	0.0343	0.033283294
		gBm	0	0.14136	0.5698	1.033	1	2.25E-244	0.52838	0.051	0	0.2877	0.0221	0.033283294
		Real	1	0.0005	3.0168	1.033	1	4.04E-241	0.52485	0.051	1	0.0067	0.0343	0.033283294
	$\Delta f_2$	Gaussian	1	0.0005	21.036	1.033	1	1.98E-246	0.5306	0.051	1	0.001	0.1316	0.033283294
		FBM	1	0.0005	2.4519	1.033	1	8.02E-239	0.52234	0.051	1	0.0074	0.0341	0.033283294
		gBm	0	0.08879	0.6511	1.033	1	5.60E-244	0.52795	0.051	0	0.2761	0.0223	0.033283294
		Real	1	0.0005	2.7622	1.033	1	1.40E-241	0.52535	0.051	0	0.0418	0.0292	0.033283294
	$\Delta P_{ie}$	Gaussian	1	0.0005	17.833	1.033	1	0	0.6246	0.051	1	0.001	0.1405	0.033283294
		FBM	0	0.05001	0.7513	1.033	1	2.95E-255	0.54004	0.051	0	0.2153	0.0234	0.033283294
		gBm	0	0.02173	0.8972	1.033	1	7.91E-284	0.56951	0.051	0	0.0146	0.0322	0.033283294
		Real	1	0.0005	2.8499	1.033	1	3.15E-290	0.5759	0.051	1	0.001	0.0463	0.033283294
$L_\infty$ Norm	$\Delta f_1$	Gaussian	1	0.0005	19.251	1.033	1	8.64E-220	0.50105	0.051	1	0.001	0.1195	0.033283294
		FBM	1	0.0005	2.4057	1.033	1	9.44E-220	0.50101	0.051	1	0.0046	0.0353	0.033283294
		gBm	1	0.0005	11.461	1.033	1	1.25E-219	0.50087	0.051	1	0.001	0.0749	0.033283294
		Real	1	0.0005	2.4351	1.033	1	1.42E-219	0.50081	0.051	1	0.0016	0.0379	0.033283294
	$\Delta f_2$	Gaussian	1	0.0005	45.097	1.033	1	8.86E-220	0.50104	0.051	1	0.001	0.1869	0.033283294
		FBM	1	0.0005	3.0605	1.033	1	9.76E-220	0.50099	0.051	1	0.001	0.0483	0.033283294
		gBm	1	0.0005	11.166	1.033	1	1.12E-219	0.50092	0.051	1	0.001	0.0754	0.033283294
		Real	1	0.0005	2.2588	1.033	1	1.32E-219	0.50084	0.051	1	0.0033	0.0362	0.033283294
	$\Delta P_{ie}$	Gaussian	1	0.0005	85.766	1.033	1	2.86E-222	0.50388	0.051	1	0.001	0.2805	0.033283294
		FBM	1	0.0005	4.1562	1.033	1	3.08E-220	0.50156	0.051	1	0.001	0.0553	0.033283294
		gBm	1	0.0005	2.414	1.033	1	5.16E-221	0.50245	0.051	1	0.001	0.0411	0.033283294
		Real	1	0.0005	4.6271	1.033	1	8.92E-221	0.50218	0.051	1	0.001	0.0616	0.033283294

**High Resolution Images**

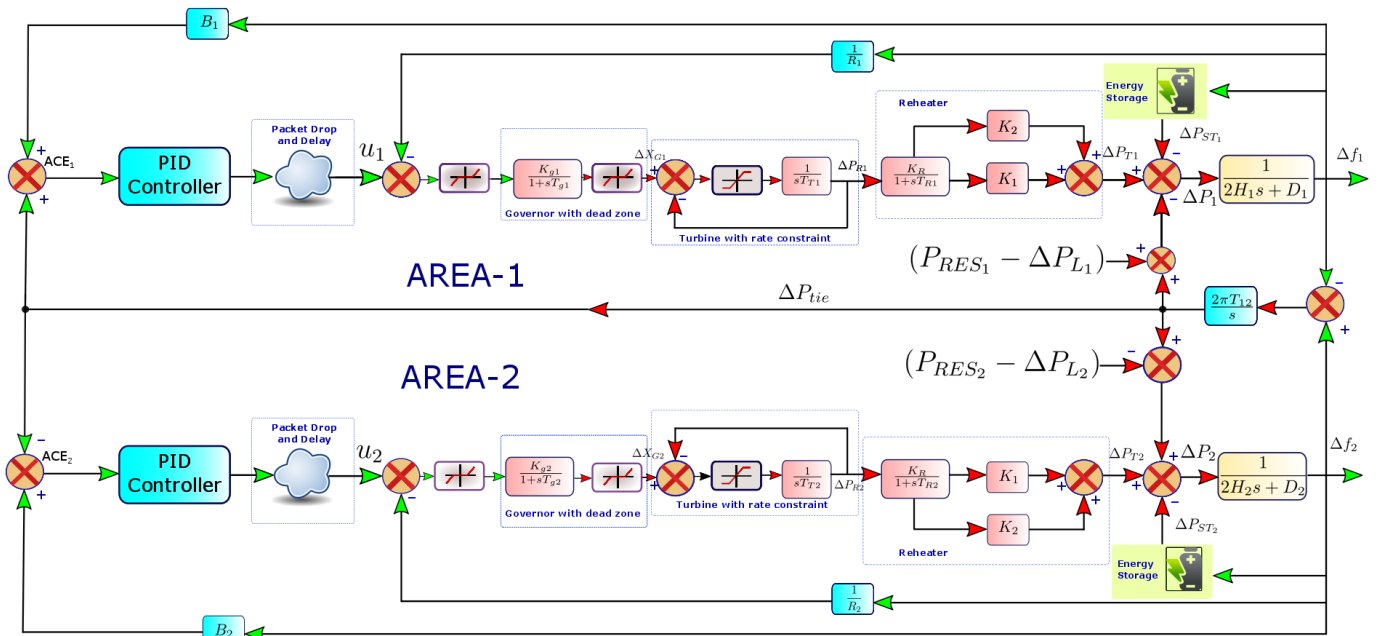


Figure 1: Schematic of the two-area LFC scheme with RES and energy storage with filtered PID controllers. The dead zones between the controller and governor increase the RES utilization in the smart grid.

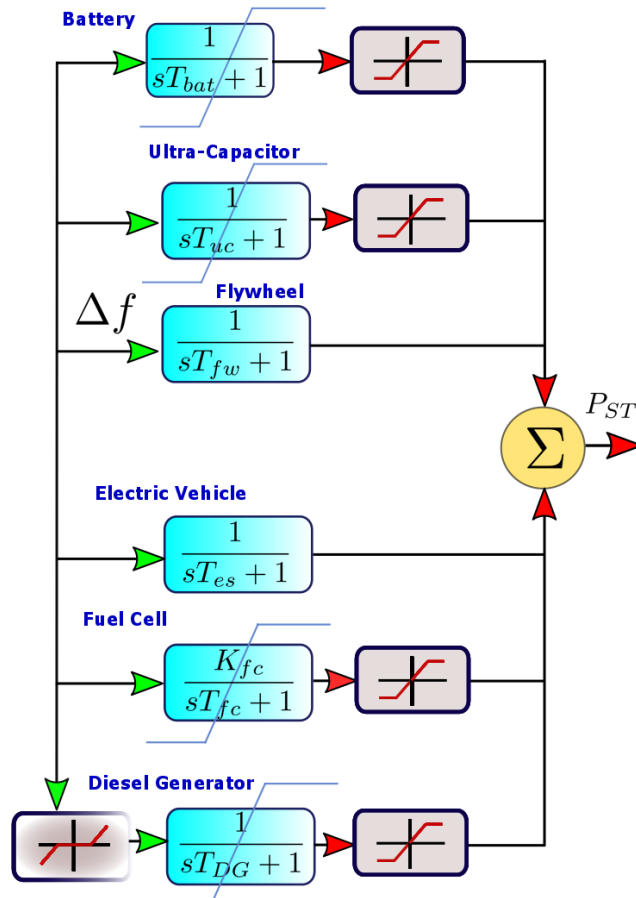


Figure 2: First order storage device models with nonlinearities like dead bands, output saturations and generation rate constraints.

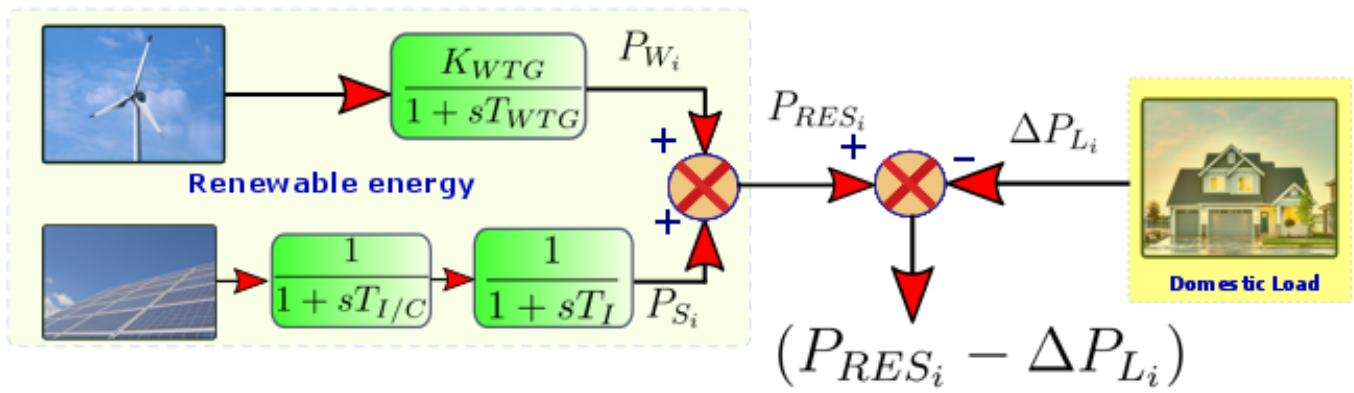


Figure 3: RES generation and load model used in the LFC scheme.

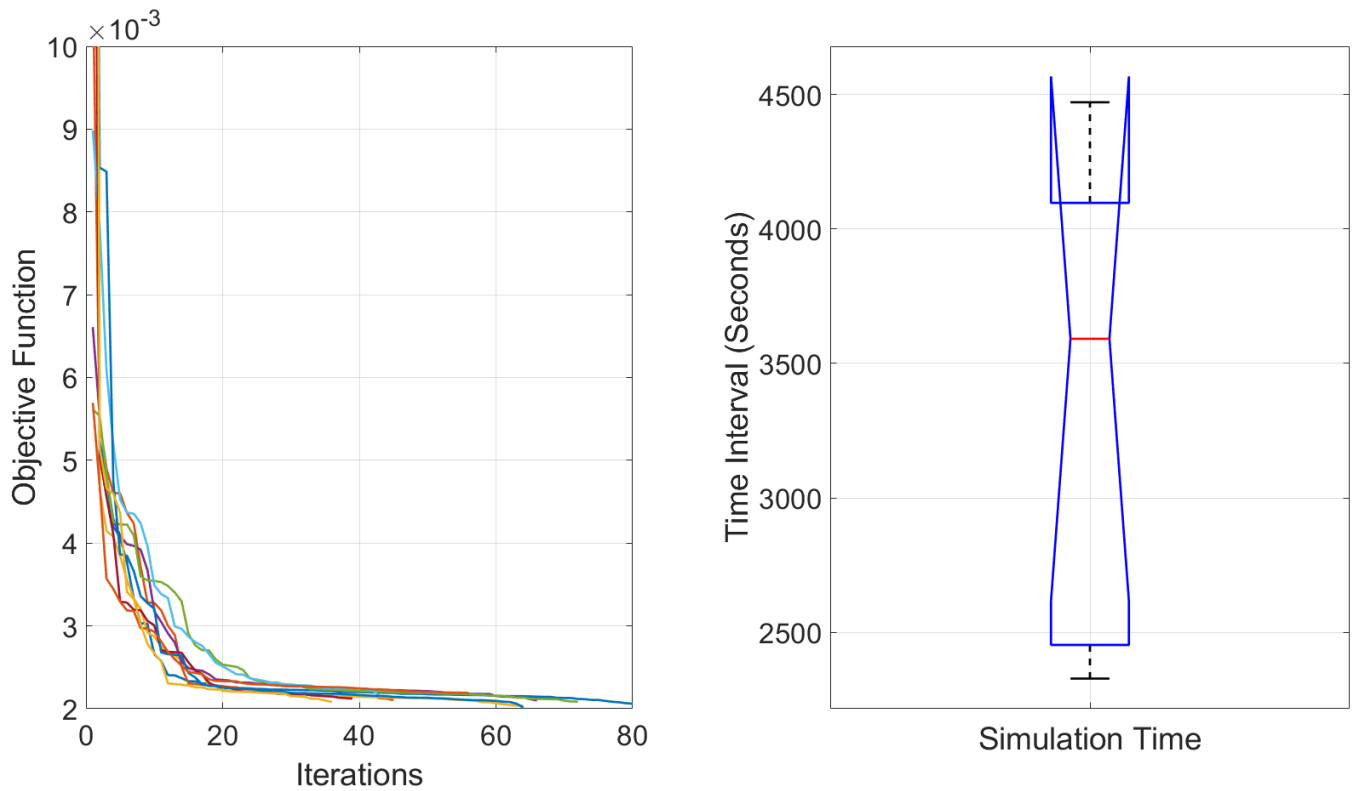


Figure 4: (left) 10 independent simulation runs of PSO and its convergence characteristics, (right) total time taken for PSO to converge.

### Controller Parameter Variation with Objective Function

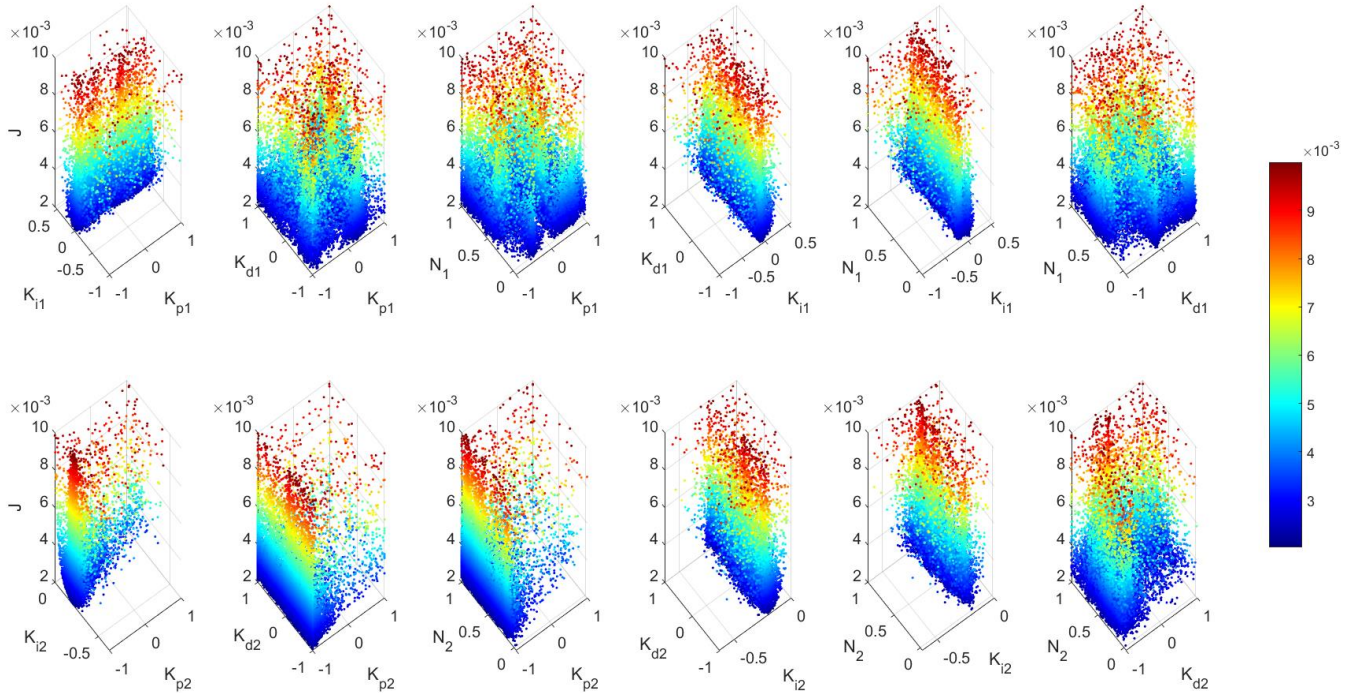


Figure 5: Convergence/bivariate distribution of the objective functions in terms of the PID controller parameters; (top panels) area 1, (bottom panels) area 2.

### Controller Parameters with Change in Iterations

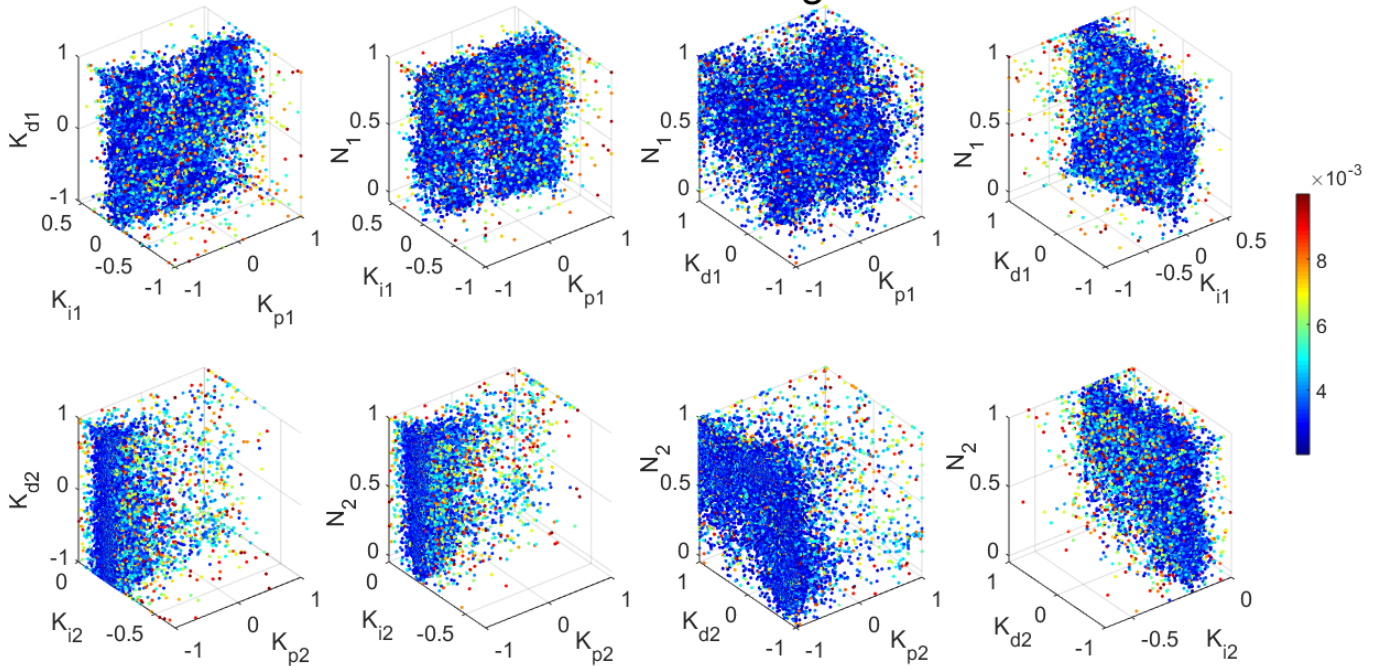


Figure 6: Multivariate distribution or feasible/stabilizable region in the PID controller parameters  $\{K_p, K_i, K_d, N\}$ . Colorbar represents ISE values.

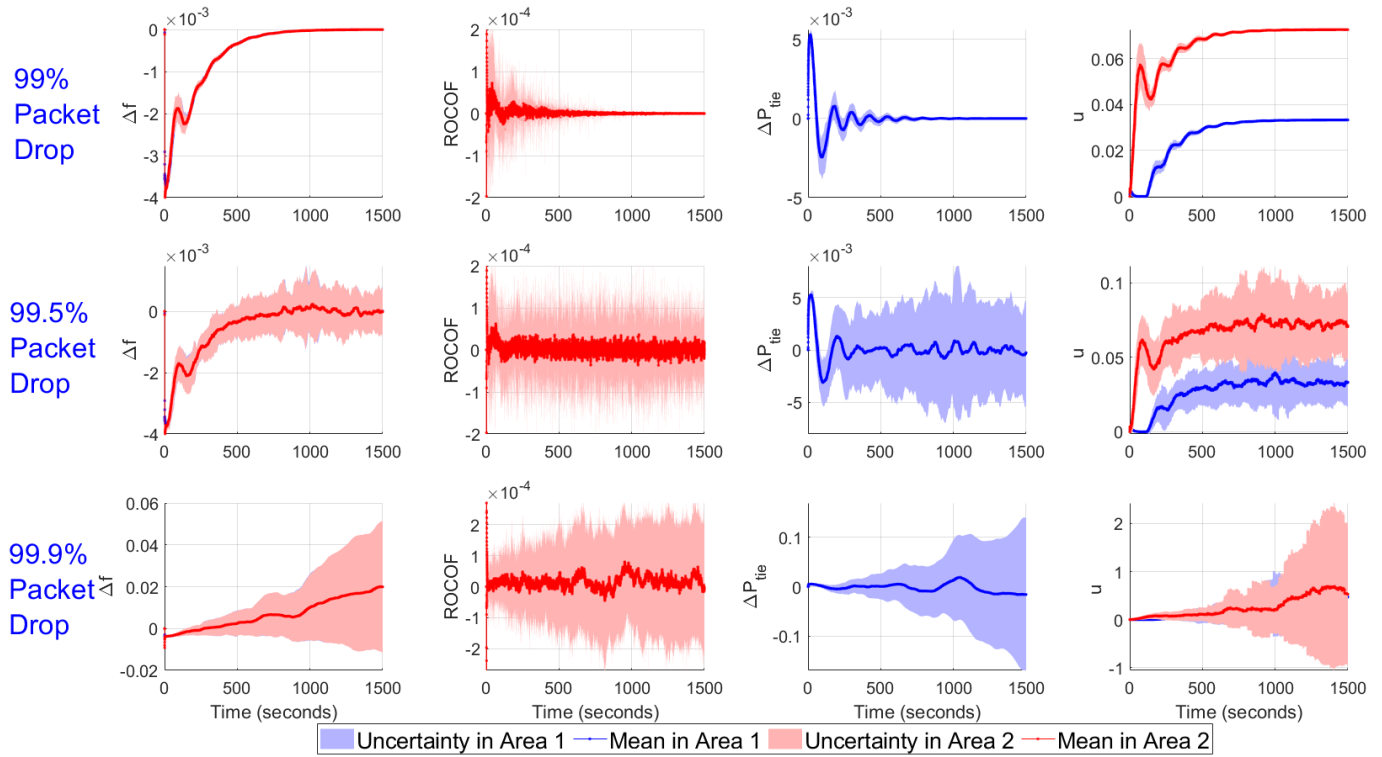
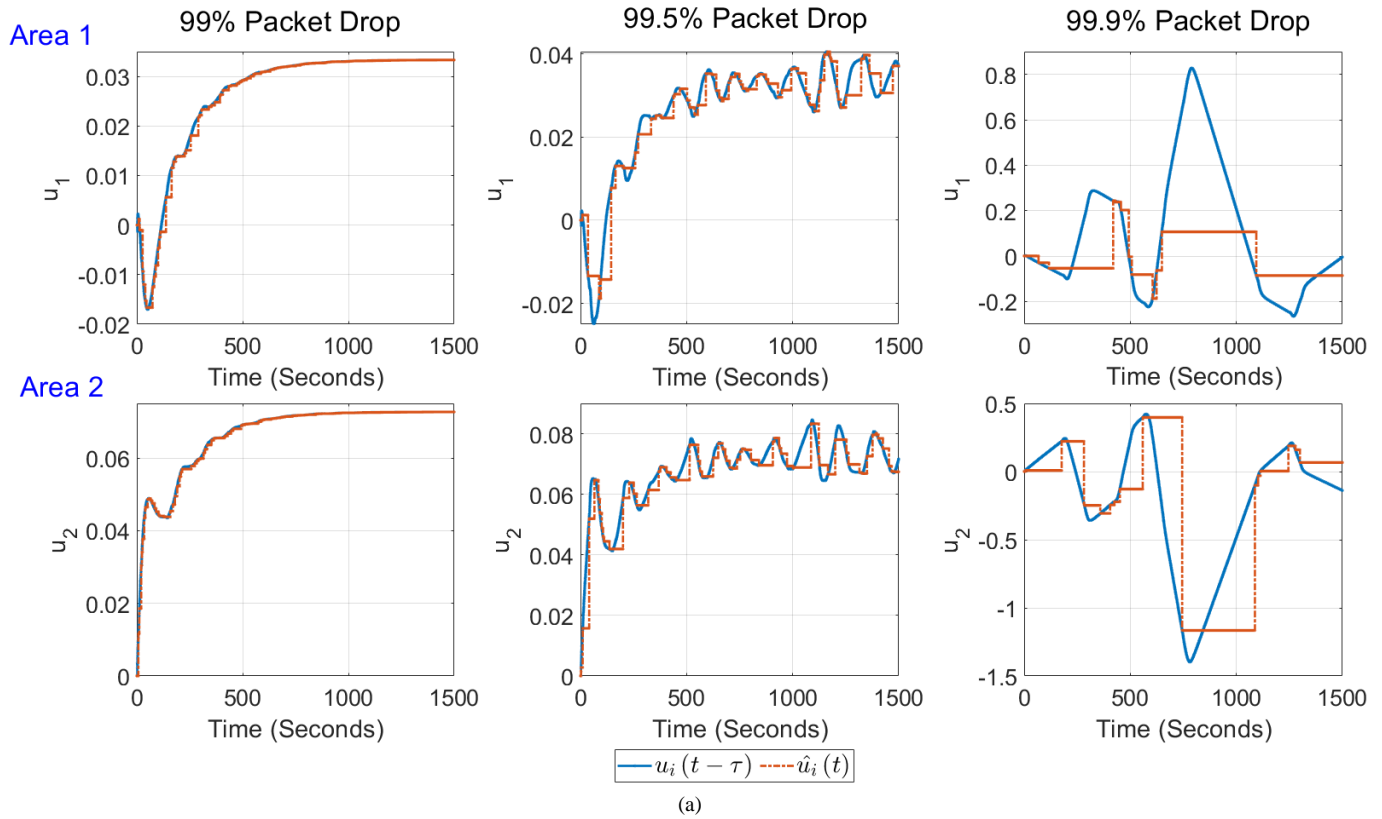
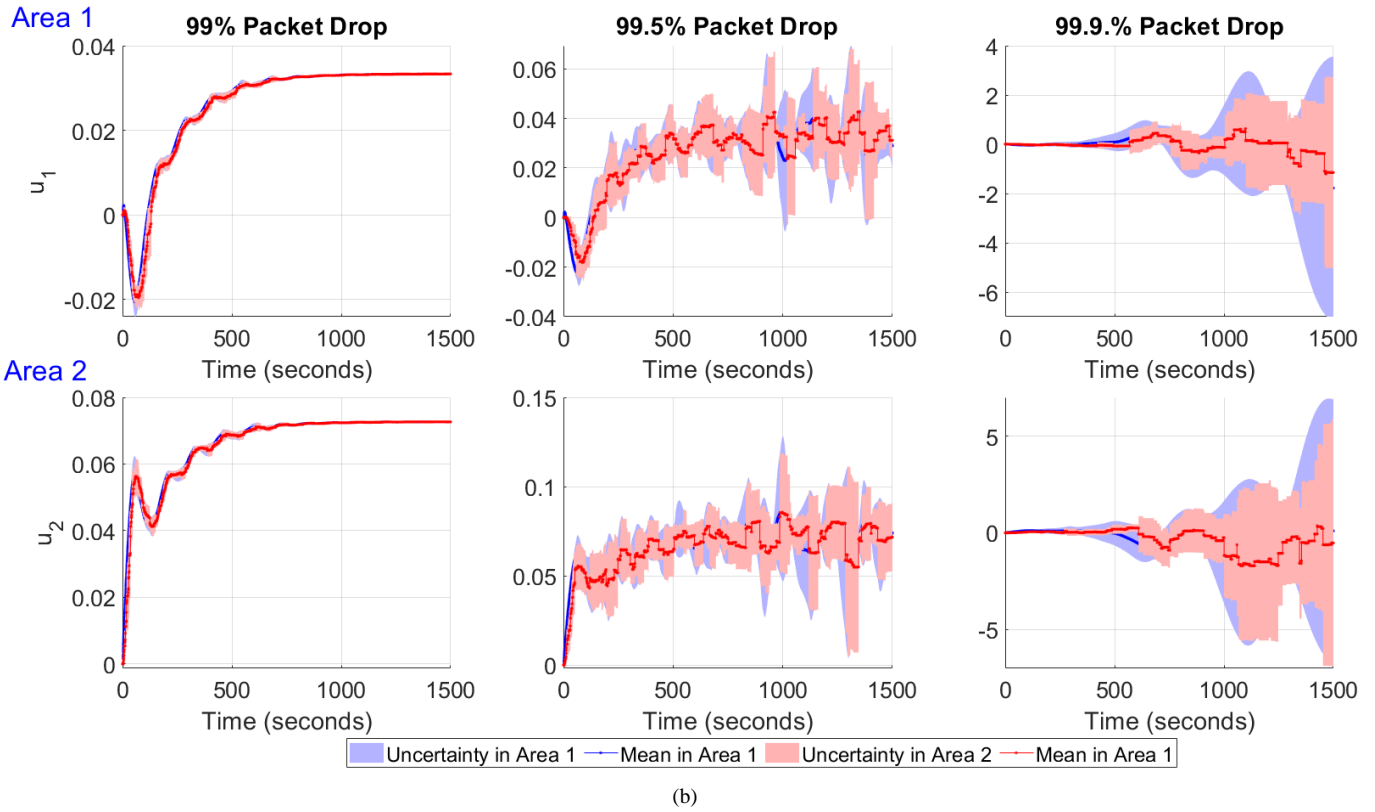


Figure 7: Step response of proposed LFC with 99%, 99.5% and 99.9% packet drops as the DoS attack on both the areas with 100 Monte Carlo simulations.





(b)  
 Figure 8: (a) Simulations of the delay-free and randomly delayed control signal for two areas with 99%, 99.5% and 99.9% packet drop. (blue)-randomly delayed control signal (red)-control signal with random delay and dropout. (b) Simulations of the delayed control signal for two areas with 99%, 99.5% and 99.9% packet drop.

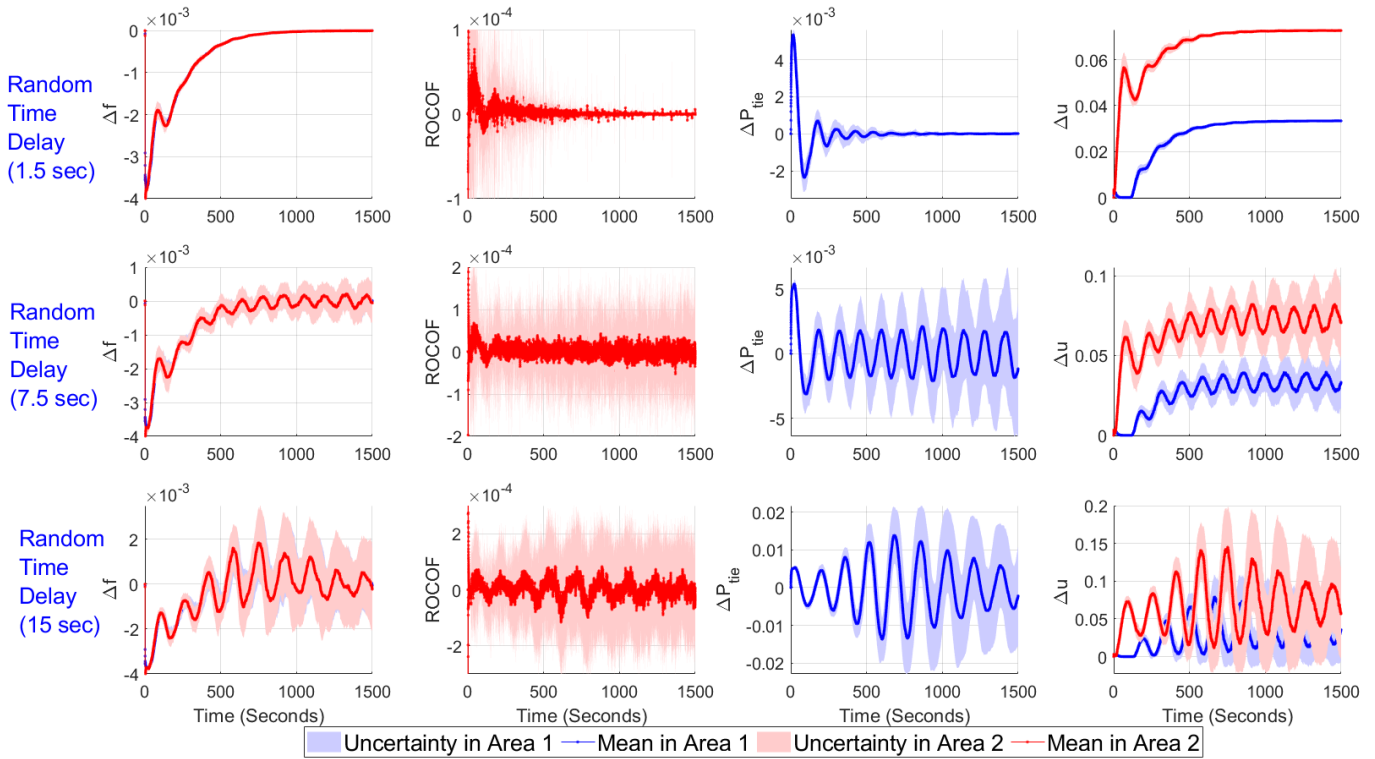


Figure 9: Step response of the LFC with  $\mu_d = 1.5$  seconds, 7.5 second and 15 seconds of random delay with 100 Monte Carlo runs.

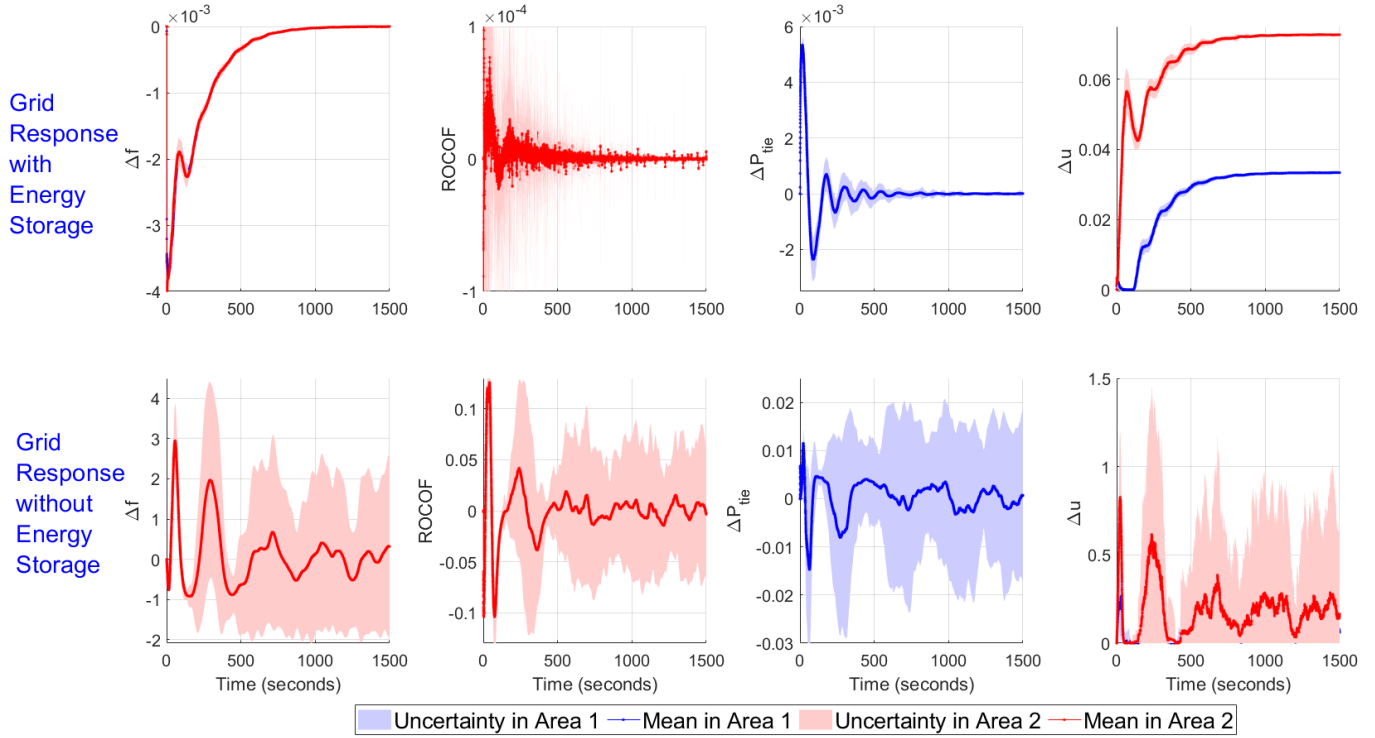


Figure 10: Step response of the system with and without energy storage elements with 100 Monte Carlo runs.

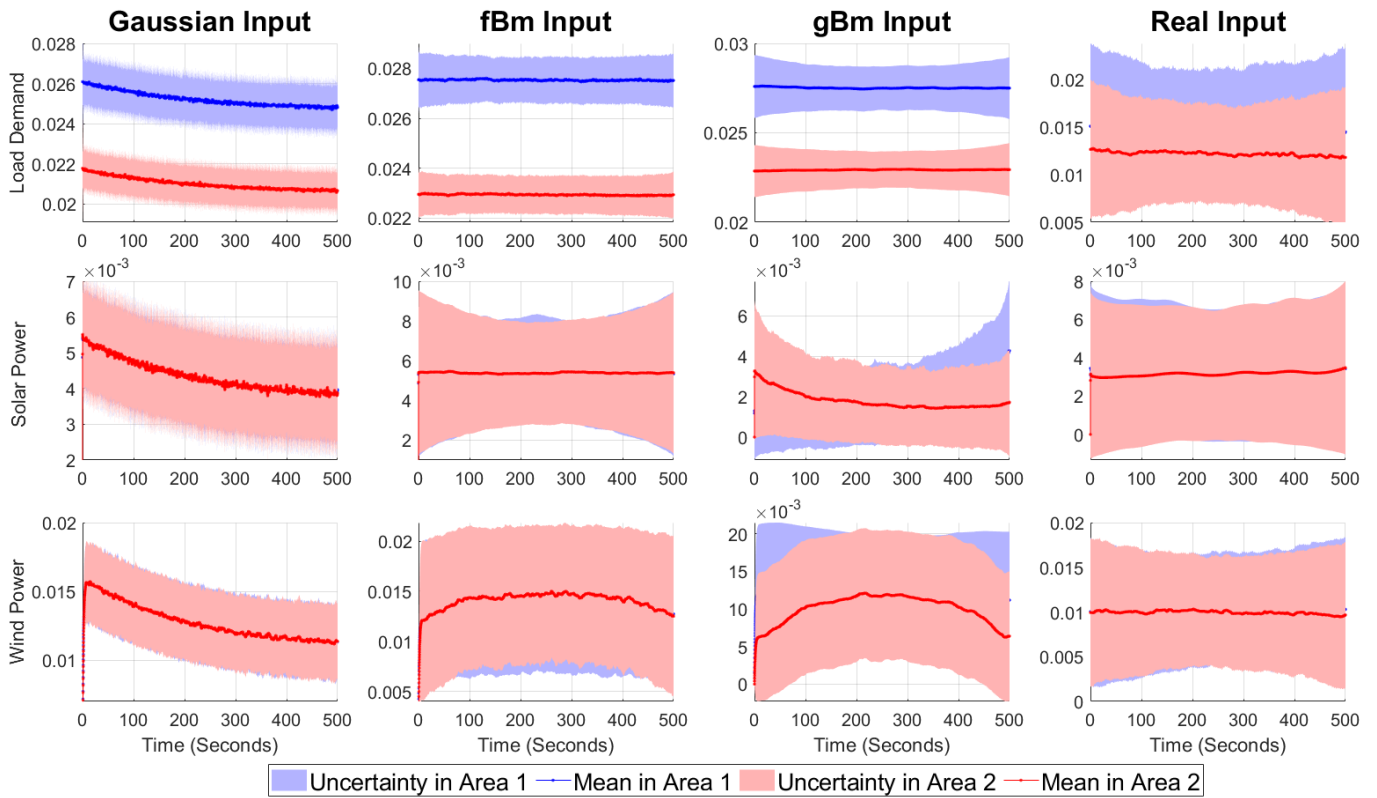


Figure 11: Stochastic input, real RES and load demand profiles for the smart grid LFC with the 100 Monte Carlo runs.

### Output Parameters for Gaussian Input Profile

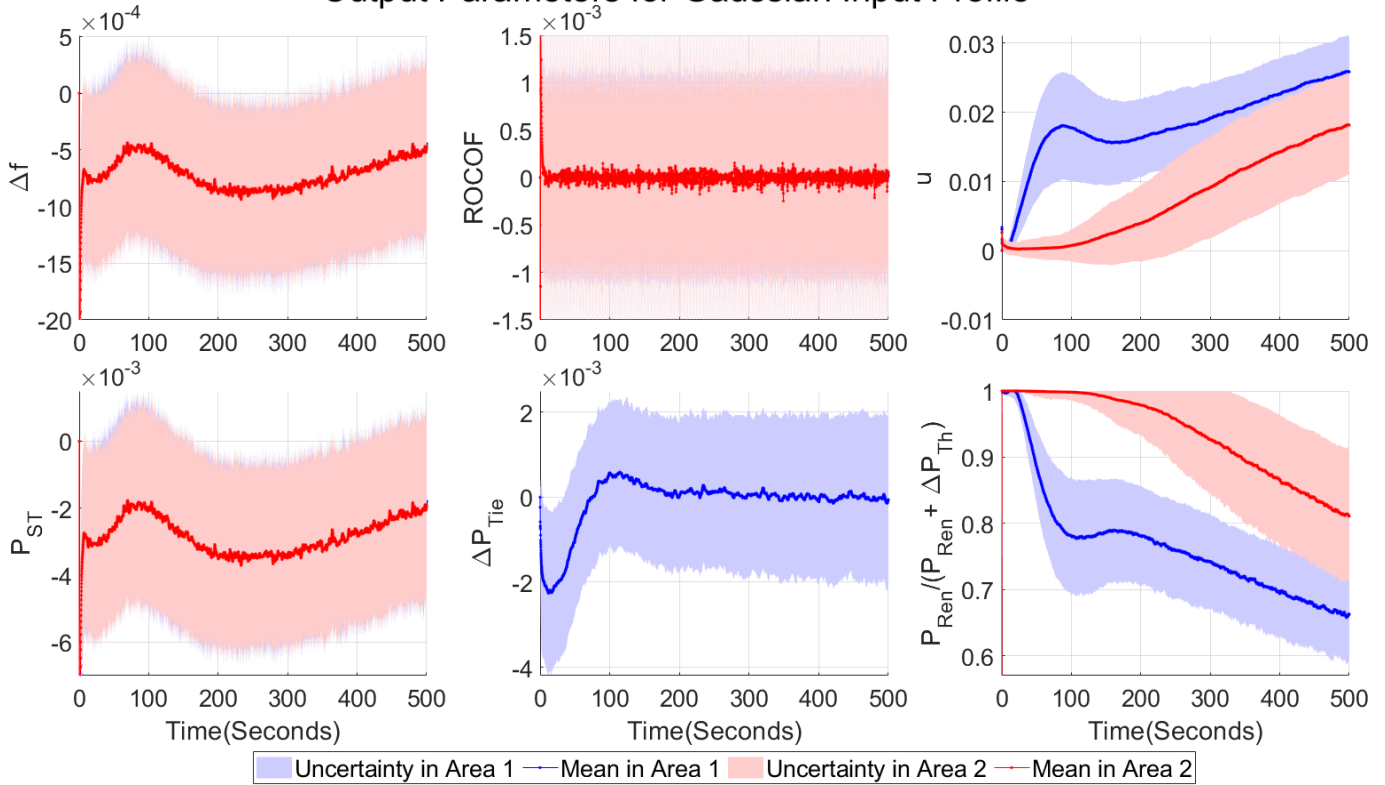


Figure 12: Smart grid performance indicators for Gaussian input profile: (top left) frequency deviation, (top center) rate of change of frequency, (top right) control input to the thermal power plant, (bottom left) energy storage output, (bottom center) tie-line power between two areas, (bottom right), proportion of renewable energy usage for the 100 Monte Carlo runs.

### Output Parameters for Fractional Brownian Motion Input Profile

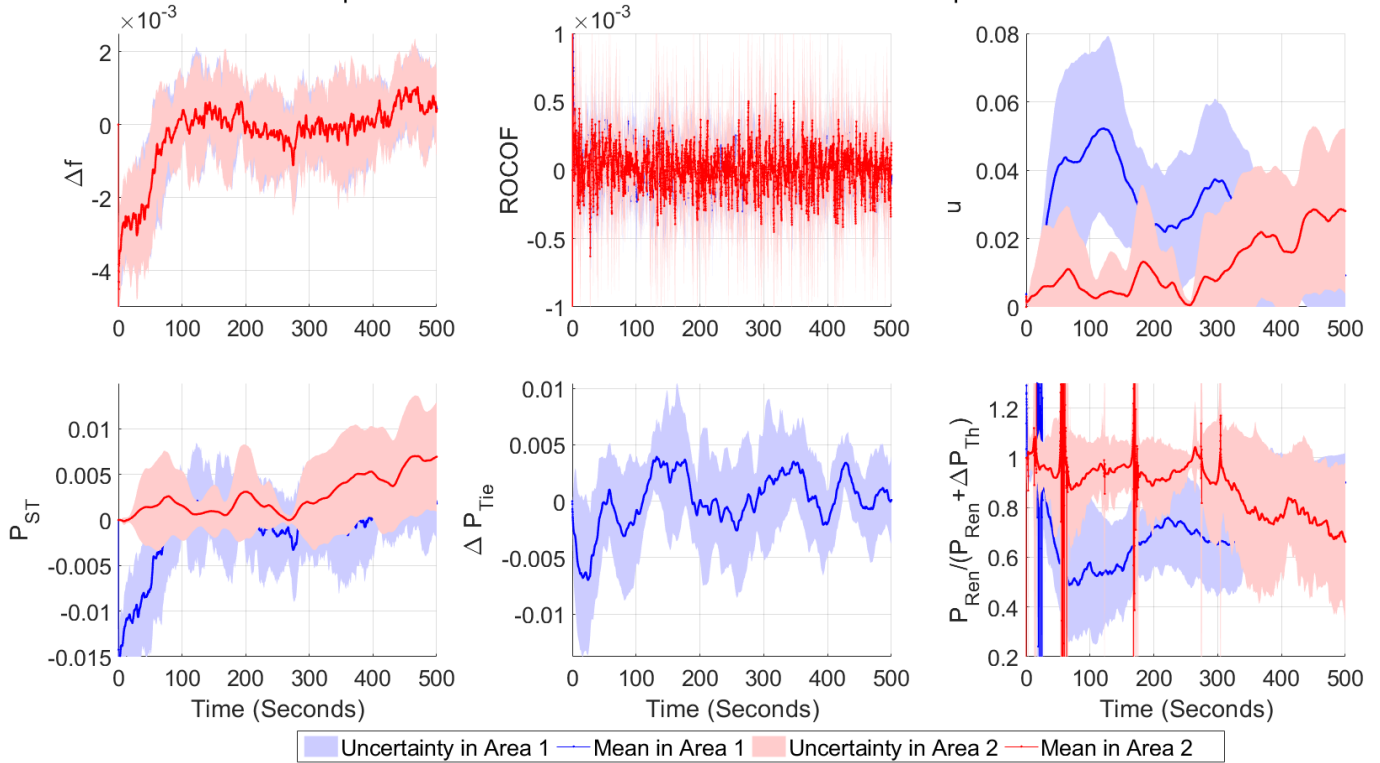


Figure 13: Smart grid performance indicators for fBm input profile: (top left) frequency deviation, (top center) rate of change of frequency, (top right) control input to the thermal power plant, (bottom left) energy storage output, (bottom center) tie-line power between two areas, (bottom right), proportion of renewable energy usage for the 100 Monte Carlo runs.



### Output Parameters for Geometric Brownian Motion Input Profile

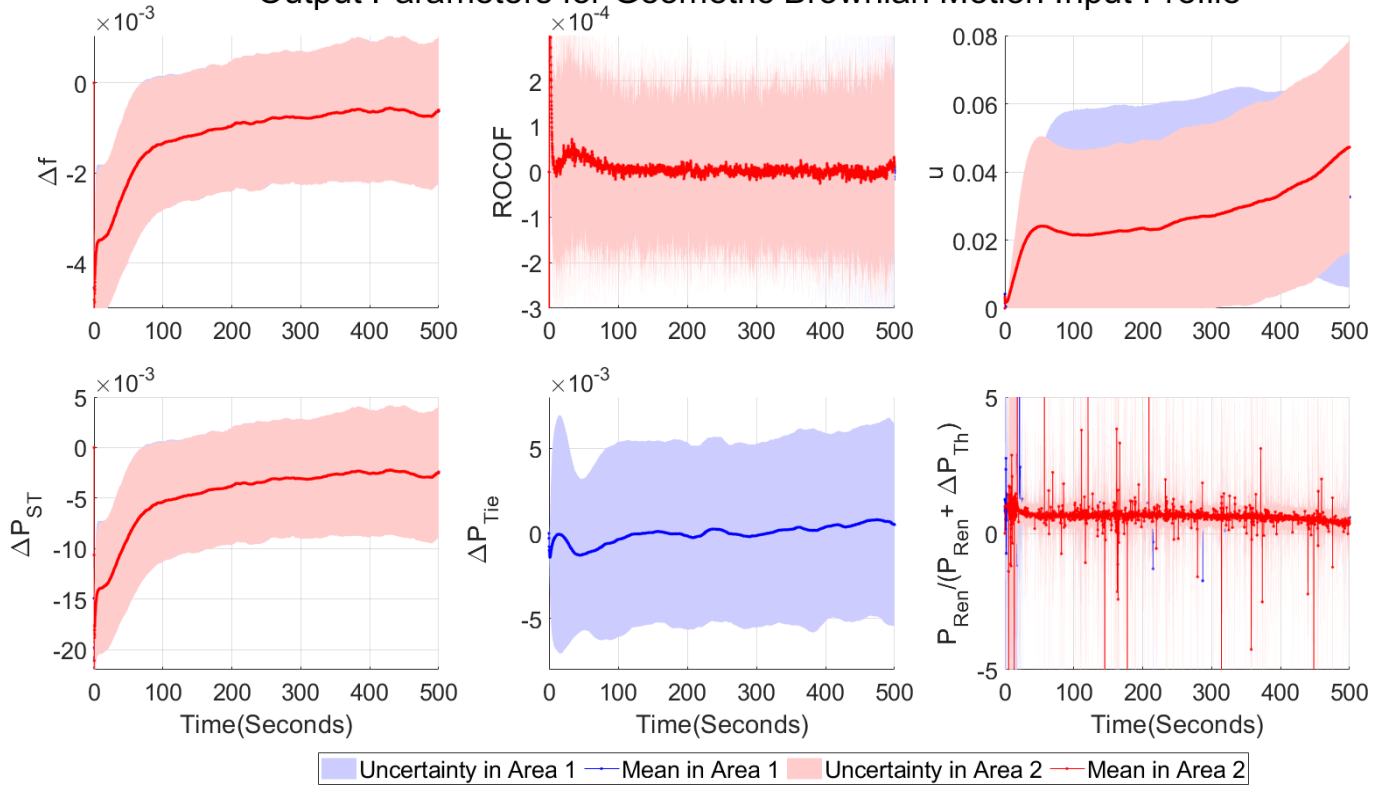


Figure 14: Smart grid performance indicators for gBm input profile (top left) frequency deviation, (top center) rate of change of frequency, (top right) control input to the thermal power plant, (bottom left) energy storage output, (bottom center) tie-line power between two areas, (bottom right) proportion of renewable energy usage for the 100 Monte Carlo runs.

### Output Parameters for Real Profiles

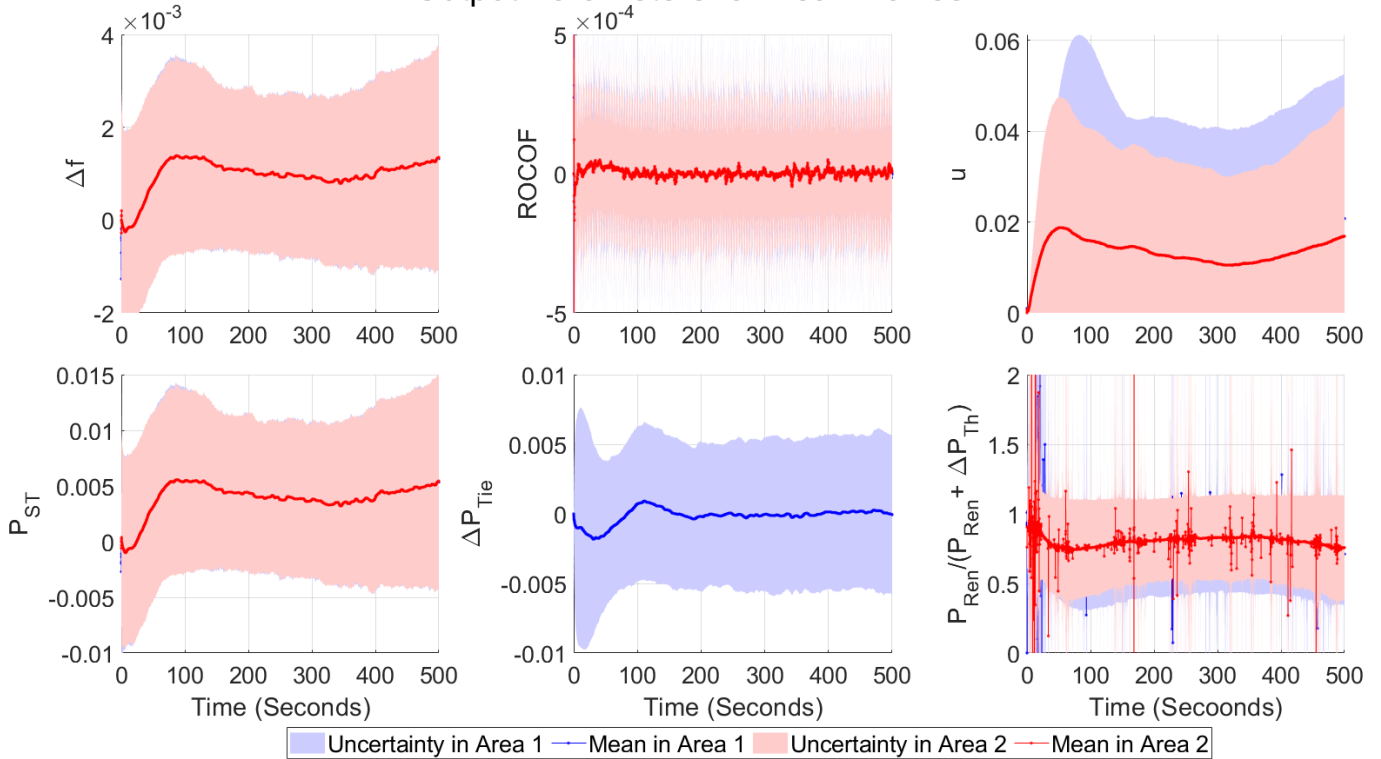


Figure 15: Smart grid performance indicators for real input profile (top left) frequency deviation, (top centre) rate of change of frequency, (top right) control input to the thermal power plant, (bottom left) energy storage output, (bottom centre) tie-line power between two areas (bottom right) proportion of renewable energy usage for the 100 Monte Carlo runs.

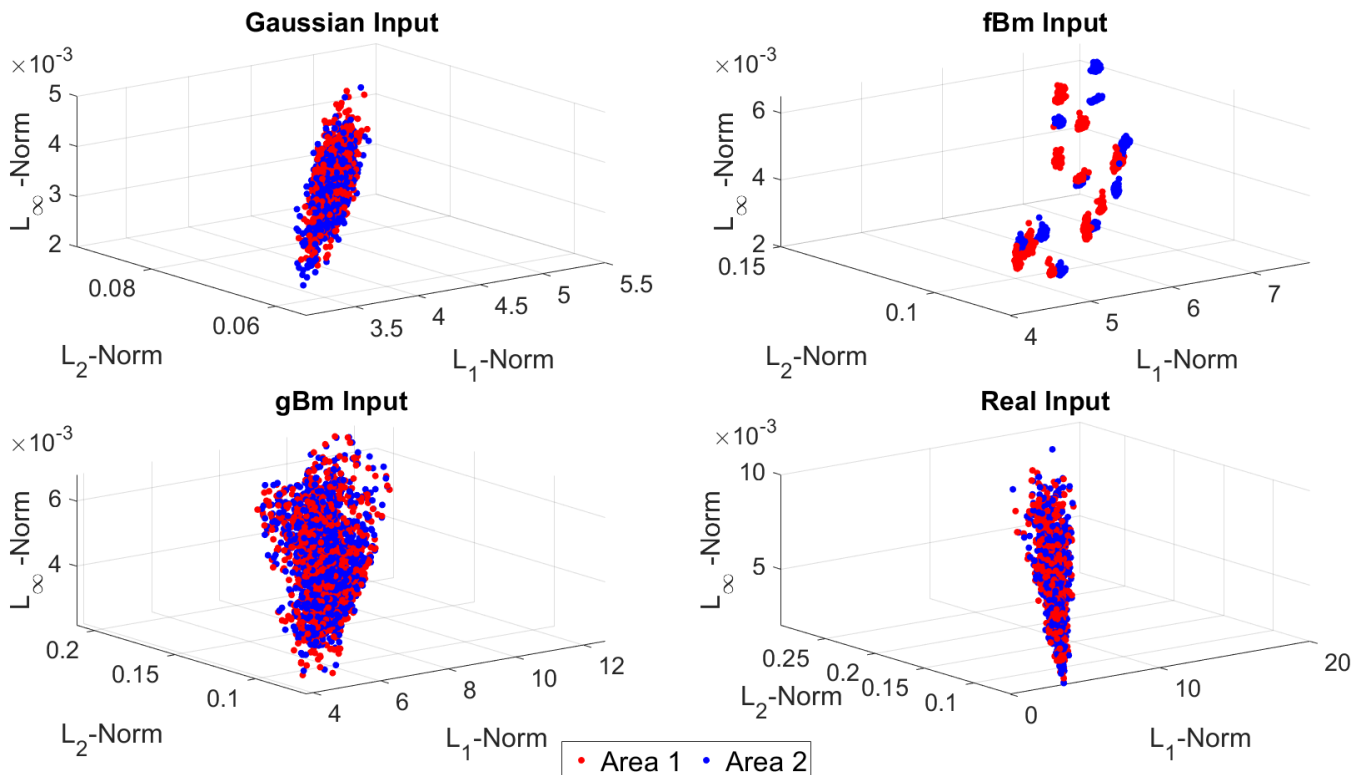


Figure 16: Scatter-plots of the  $L_1$ ,  $L_2$  and  $L_\infty$  norms of the frequency fluctuations with different RNGs: (left top) Gaussian inputs, (left-right) fBm inputs, (left bottom) gBm inputs, (right bottom) real inputs.

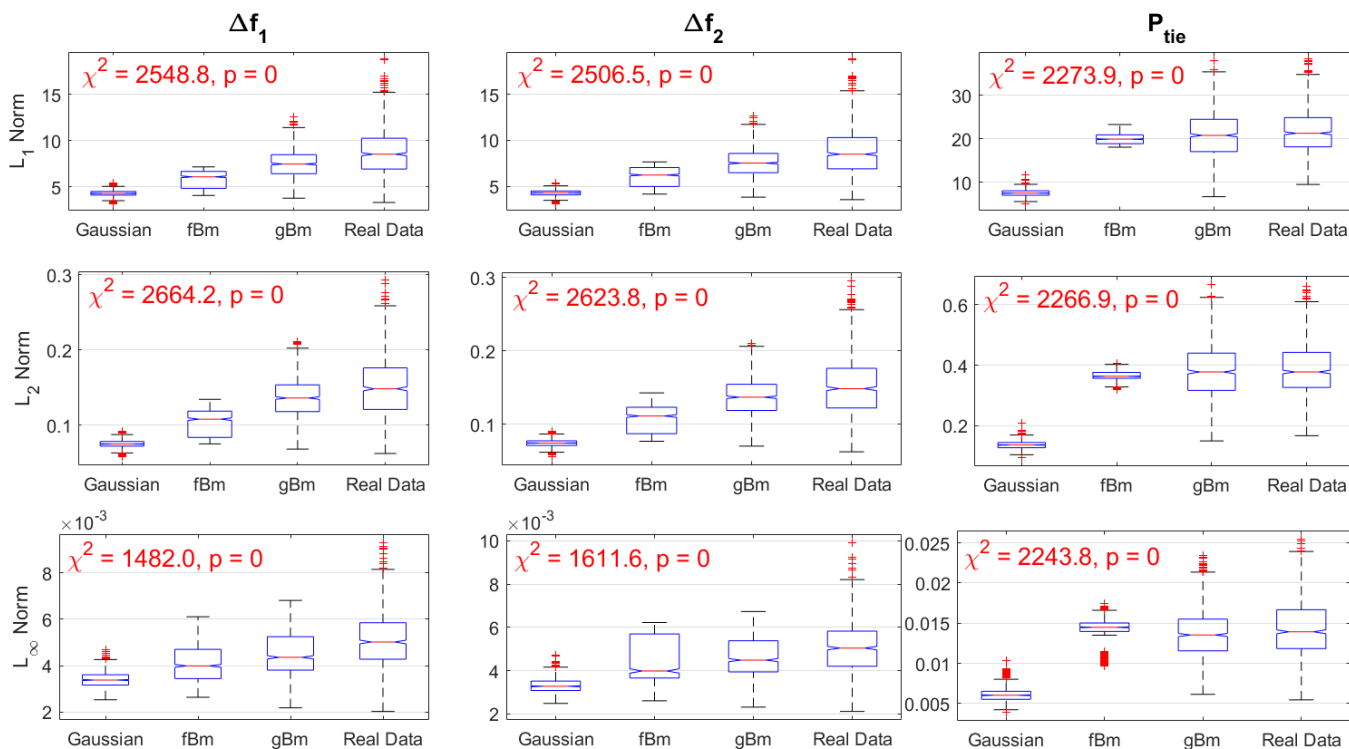


Figure 17: Box-plots of the  $L_1$ ,  $L_2$  and  $L_\infty$  norms of the frequency fluctuations in the two areas and tie-line power exchange for different input profiles. The  $p$ -values are also reported for each case using the Kruskal-Wallis test.

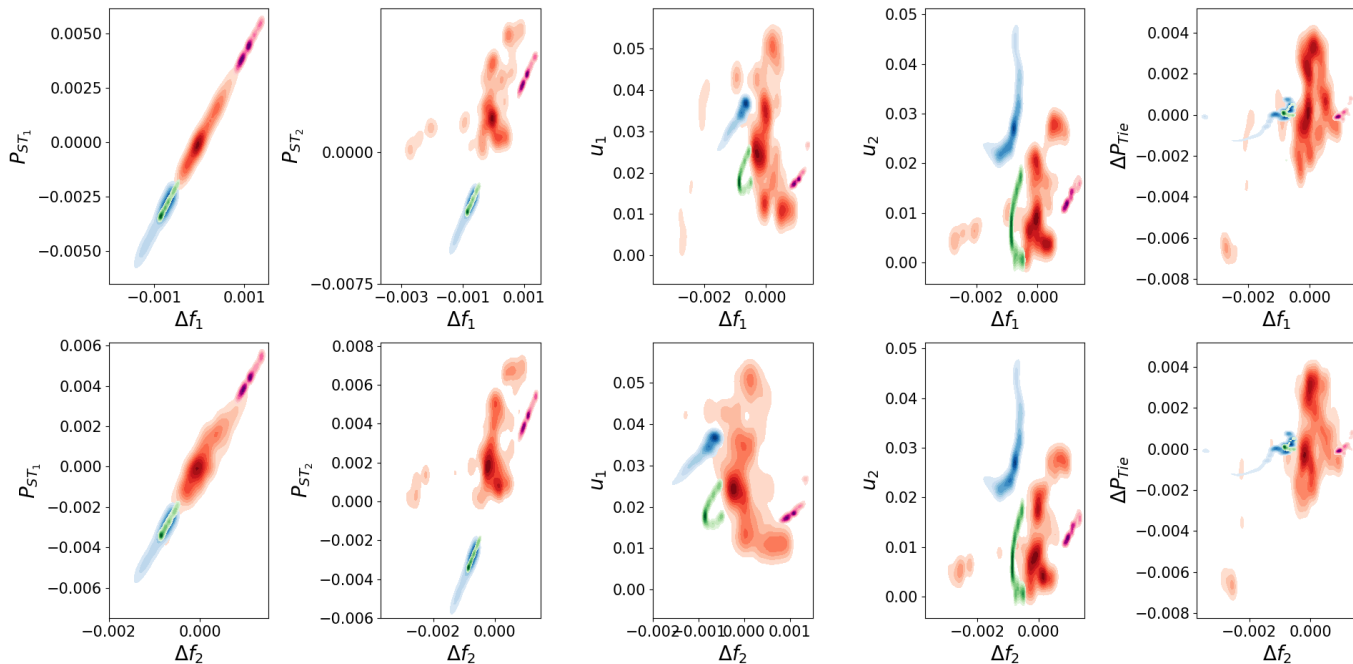


Figure 18: Multivariate KDE plots of the grid parameters with the frequency fluctuations in each area. The colors represent different RNGs: red = fBm, green = Gaussian, blue = gBm, magenta = real data.

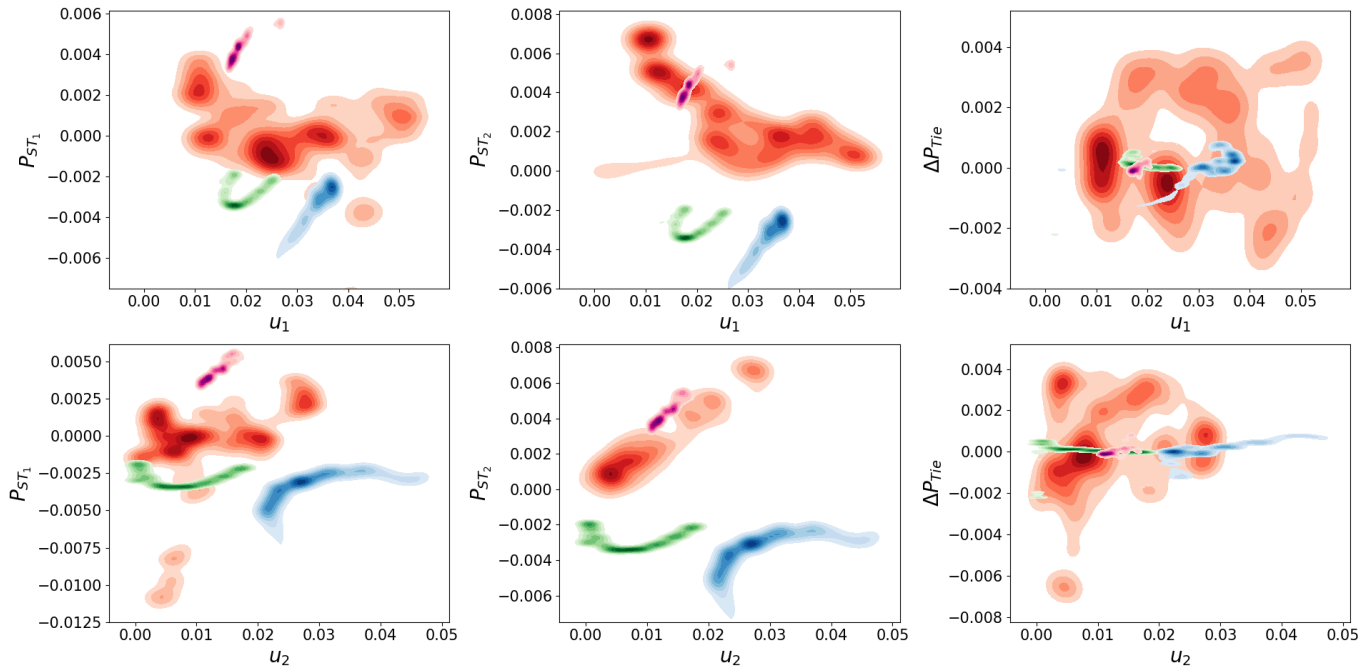


Figure 19: Multivariate KDE plots of the energy storage operation, tie-line power with the control input to the governor in two areas. The colors represent different RNGs: red = fBm, green = Gaussian, blue = gBm, magenta = real data.

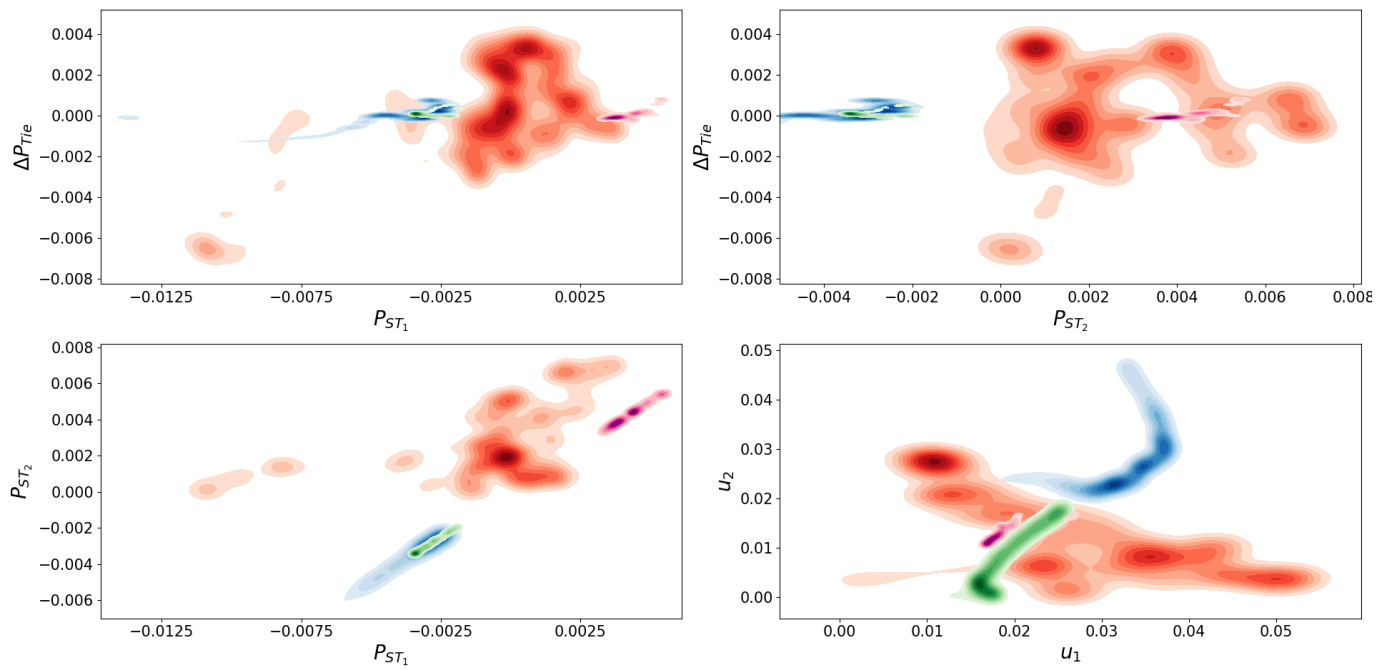


Figure 20: Multivariate KDE plot of (a) Tie-line power and storage operation in area 1 (top-left) (b) Tie-line power and storage operation in area 2 (top-right) (c) Storage operation in both the areas (bottom-left) (d) Control input for both the areas (bottom-right). The colors represent different RNGs: red = fBm, green = Gaussian, blue = gBm, magenta = real data.